iScience

CellPress
OPEN ACCESS

Article

Mitochondrial Bcl-xL promotes brain synaptogenesis by controlling non-lethal caspase activation

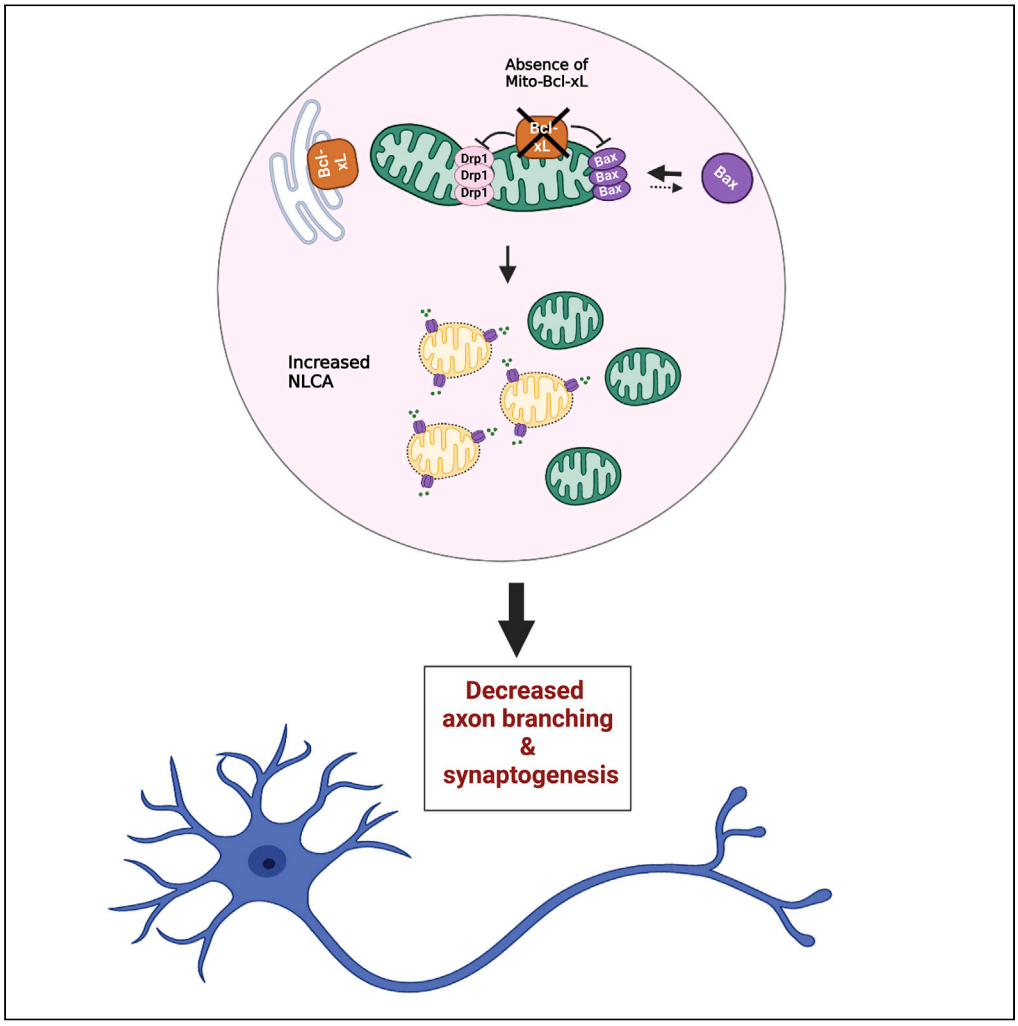

Trang Thi Minh Nguyen, Rudy Gadet, Marine Lanfranchi, ..., Frédéric Saudou, Nikolay Popgeorgiev, Germain Gillet

germain.gillet@univ-lyon1.fr

Highlights

The exclusive loss of mitochondrial Bcl-xL does not prevent mouse development and birth

KI mice expressing ER-based Bcl-xL die soon postpartum, evoking the 22q11DS syndrome

Bcl-xL fosters synaptogenesis through non-lethal caspase activation

Nguyen et al., iScience 26, 106674
May 19, 2023
https://doi.org/10.1016/j.isci.2023.106674

iScience

CellPress
OPEN ACCESS

Article

Mitochondrial Bcl-xL promotes brain synaptogenesis by controlling non-lethal caspase activation

Trang Thi Minh Nguyen,[1] Rudy Gadet,[1] Marine Lanfranchi,[2] Romane A. Lahaye,[3] Sozerko Yandiev,[2] Olivier Lohez,[1] Ivan Mikaelian,[1] Lea Jabbour,[1] Ruth Rimokh,[1] Julien Courchet,[2] Frédéric Saudou,[3] Nikolay Popgeorgiev,[1,4,6] and Germain Gillet[1,5,7,*]

SUMMARY

Non-lethal caspase activation (NLCA) has been linked to neurodevelopmental processes. However, how neurons control NLCA remains elusive. Here, we focused on Bcl-xL, a Bcl-2 homolog regulating caspase activation through the mitochondria. We generated a mouse model, referred to as ER-xL, in which Bcl-xL is absent in the mitochondria, yet present in the endoplasmic reticulum. Unlike *bclx* knockout mice that died at E13.5, ER-xL mice survived embryonic development but died post-partum because of altered feeding behavior. Enhanced caspase-3 activity was observed in the brain and the spinal cord white matter, but not the gray matter. No increase in cell death was observed in ER-xL cortical neurons, suggesting that the observed caspase-3 activation was apoptosis-independent. ER-xL neurons displayed increased caspase-3 activity in the neurites, resulting in impaired axon arborescence and synaptogenesis. Together, our findings suggest that mitochondrial Bcl-xL finely tunes caspase-3 through Drp-1-dependent mitochondrial fission, which is critical to neural network design.

INTRODUCTION

Bcl-2 proteins have been widely studied for their role in the regulation of apoptosis. These proteins control the activation of cysteine-dependent aspartate-directed proteases (caspases) by regulating the release of apoptogenic factors from the mitochondria to the cytosol in a process called mitochondrial outer membrane permeabilization (MOMP).[1,2] Notably, MOMP is initiated through the oligomerization of pro-apoptotic effectors Bax and Bak, which is repressed by the anti-apoptotic Bcl-2 proteins. Dysregulation of this finely tuned equilibrium between cell death and survival occurs in a number of pathologies, including developmental defects, degenerative diseases, and cancers.[3–5]

The Bcl-xL protein is a Bcl-2 homolog with a key role in embryonic development. In the mammalian embryo, its expression is ubiquitous, and particularly high levels have been measured in the nervous system.[6,7] Invalidation of the *bclx* gene in mice causes early embryonic death (E13.5), which has been attributed to increased apoptosis in the nervous and hematopoietic systems.[8] Furthermore, although Bcl-xL has a mitochondrial localization, it is also found in the endoplasmic reticulum (ER), where it participates in the regulation of IP_3-dependent intracellular Ca^{2+} trafficking.[9,10]

To investigate the impact of intracellular partitioning of Bcl-xL during development, we used a knock-in (KI) strategy in mice to selectively remove Bcl-xL protein from mitochondria, its presence being maintained in the ER.

Here, we report that the loss of Bcl-xL exclusively in the mitochondria does not hinder embryonic development and birth. However, homozygous mutant mice (referred to as ER-xL) died on postnatal day 1 (P1), displaying swallowing and feeding defects reminiscent of the 22q11DS genetic syndrome. Histochemical analyses performed at embryonic stage E13.5 revealed an increase in caspase-3 activity in the spinal cord, the brain stem and the cortex. Caspase-3 staining was intense and homogeneous in the white matter, but sparse in the gray matter, suggesting an impact on neurites but not on the cell body. Cultures of primary

[1]Université de Lyon, Université Claude Bernard Lyon 1, INSERM 1052, CNRS UMR 5286, Centre Léon Bérard, Centre de recherche en cancérologie de Lyon, 69008 Lyon, France

[2]Université de Lyon, Université Claude Bernard Lyon 1, Physiopathologie et Génétique du Neurone et du Muscle, UMR 5261, INSERM U 1315, Institut NeuroMyoGène, 69008 Lyon, France

[3]Grenoble Institut des Neurosciences, Université Grenoble Alpes, Inserm U1216, 38700 La Tronche, France

[4]Institut Universitaire de France (IUF), 75231 Paris Cedex 5, France

[5]Hospices civils de Lyon, Laboratoire d'anatomie et cytologie pathologiques, Centre Hospitalier Lyon Sud, chemin du Grand Revoyet, 69495 Pierre Bénite, France

[6]Senior author

[7]Lead contact

*Correspondence: germain.gillet@univ-lyon1.fr

https://doi.org/10.1016/j.isci.2023.106674

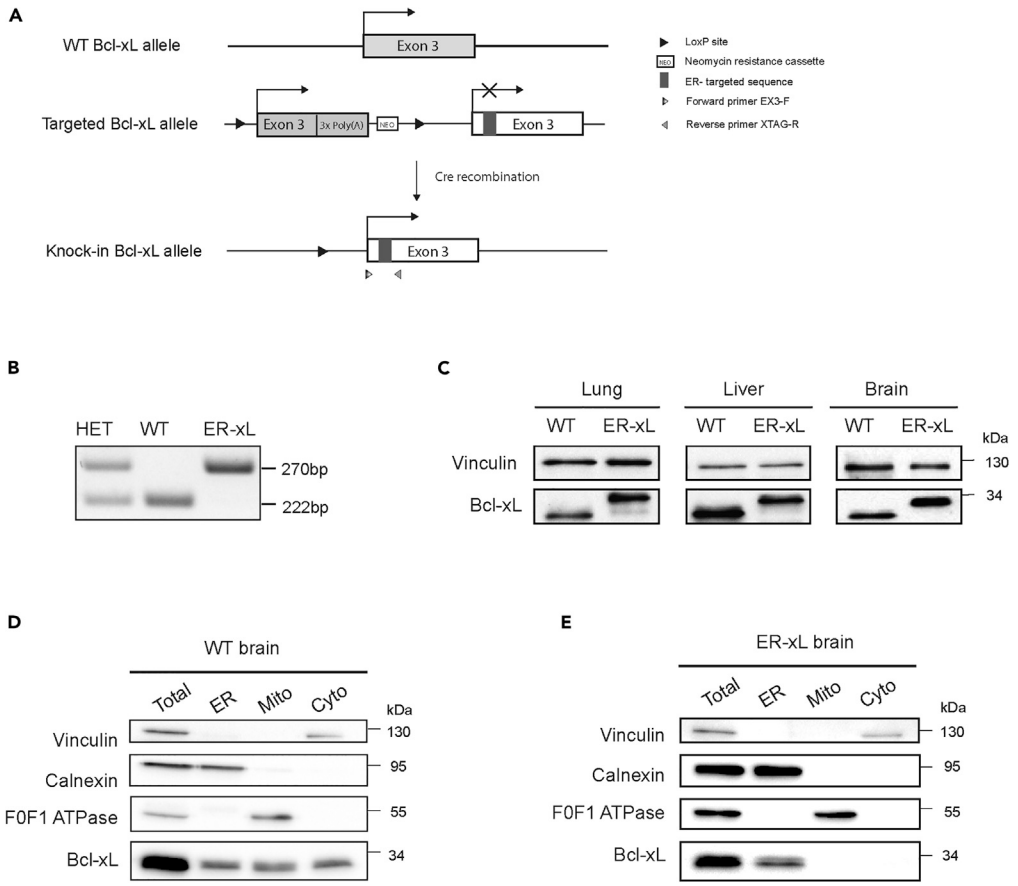

Figure 1. Generation and characterization of ER-xL mice

(A) Schematic representation of the gene targeting strategy: an engineered vector containing a WT Bcl-xL exon 3 (E3) flanked by two *LoxP* sites, and a modified E3 targeting ER were inserted to replace WT Bcl-xL E3 in floxed mice. Cre recombination induced WT E3 and allowed ER-targeted E3 expression. The sites of EX3-F and XTAG-R for PCR genotyping are shown.

(B) PCR genotyping of WT, ER-xL, and heterozygous mice. The 270-bp band indicates the presence of the ER-targeted E3 allele, while the 222-bp band indicates the presence of WT E3.

(C) Expression of the Bcl-xL protein in the lung, liver, and brain tissues of WT and ER-xL mice. Western blot analysis was performed with indicated antibodies. Vinculin was used as a loading control.

(D and E) Expression of the Bcl-xL protein in the subcellular fractions of ER, mitochondria, and cytosol from postnatal P1 brain of WT (D) and ER-xL (E) mice. Western blot analysis was performed with indicated antibodies. Vinculin was used as a cytosolic marker, calnexin as an ER marker, and F0F1 ATPase as a mitochondrial marker.

ER-xL neurons derived from the cortex confirmed that the loss of mitochondrial Bcl-xL leads to caspase-3 activation in the neurites, without a significant increase in apoptosis.

Collectively, our data indicate that such non-lethal caspase activation (NLCA) impacts neurite outgrowth and synaptic connections. These data suggest that Bcl-xL controls local activation of caspase-3 in the neurites to ensure neuronal development. Hence, our findings offer new perspectives regarding the role of Bcl-xL in development and in neurodegenerative diseases.

RESULTS

Generation of ER-Bcl-xL mice

Bcl-xL actively cycles between the cytosol and the mitochondria, and was also shown to locate at ER membranes. Through these different locations, Bcl-xL performs a variety of functions, beyond apoptosis control. To assess the respective contribution of the subcellular pools of Bcl-xL to embryonic development, we

A

B

		Died before 12h	Died at 12-24h	Survival to 24h	Total
Normal condition	WT	0 (0%)	0 (0%)	10 (100%)	10
	ER-xL	5 (71.4%)	2 (28.6%)	0 (0%)	7
Artificial feeding	WT	0 (0%)	0 (0%)	10 (100%)	10
	ER-xL	3 (42.8%)	3 (42.8%)	1 (14.3%)	7

C

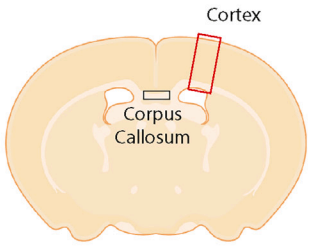

D

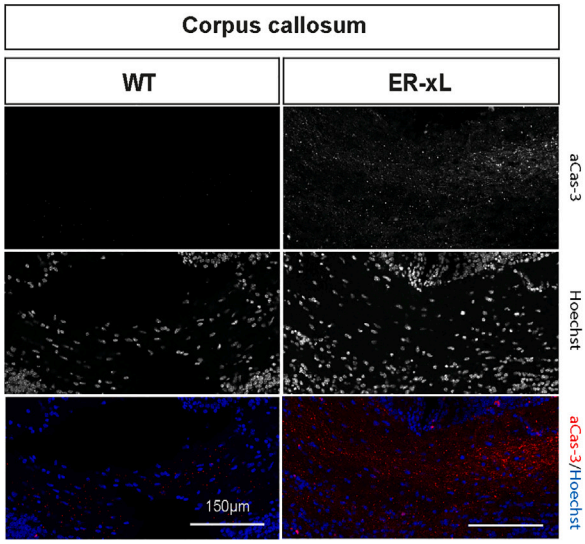

E

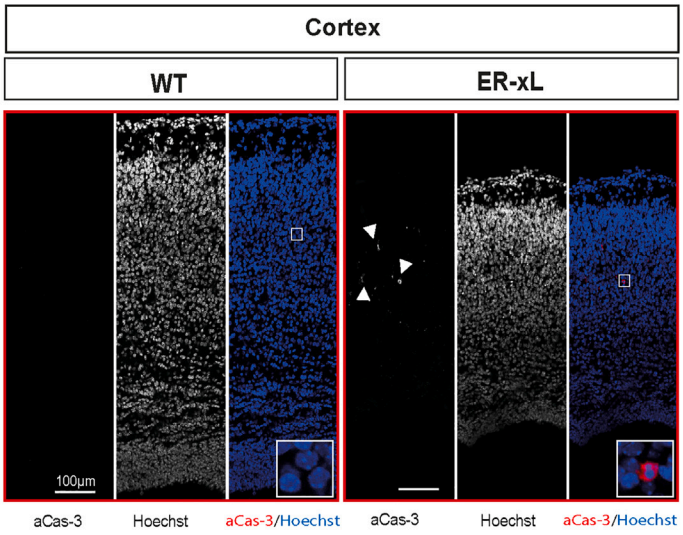

F

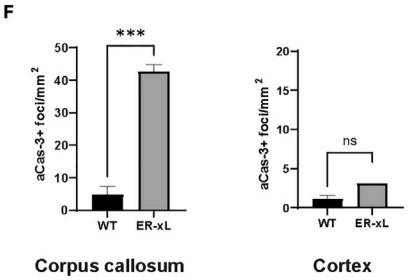

G

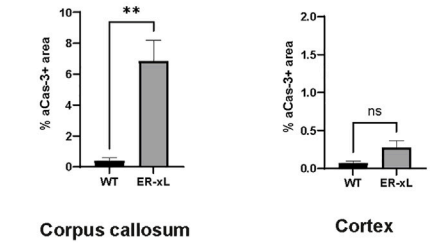

Figure 2. Characterization of ER-xL mouse phenotype

(A) Image of newborn WT and ER-xL mice (phenotype of each mouse is indicated). The milk pocket is visible in the WT newborn (red circle).

(B) Table showing number of dead and live ER-xL, HET, and WT newborns over the first 24 h with normal conditions (with mother mouse) or with artificial feeding.

(C) Illustration of the relative position in the whole coronal brain section of high magnification images in (D-E).

(D and E) Representative high-magnification images of the corpus callosum (D) and cortex (E). Immunofluorescence was performed with active caspase-3 (aCas-3). Arrowheads point to active caspase-3-positive cell bodies. Nuclei were marked with Hoechst 33342.

(F) Quantification of active caspase-3 foci density in the WT and ER-xL corpus callosum and cortex. Data show average value ±SEM. Data are from three independent experiments. Student's *t* test. $N_{WT} = 3$, $N_{ER\text{-}xL} = 3$.

(G) Percentage of surface area with active caspase-3 in the WT and ER-xL corpus callosum and cortex. Data show average value ±SEM. Data are from three independent experiments. Student's *t* test. $N_{WT} = 3$, $N_{ER\text{-}xL} = 3$.*p<0.05; **p<0.01; ***p<0.001.

generated a KI mouse strain (herein referred to as ER-xL), expressing a recombinant Bcl-xL protein exclusively in the ER. Based on the Cre/LoxP technology, we targeted the exon 3 (E3) in the wild-type (WT) allele. *Bclx* E3 encodes the C-terminus transmembrane (TM) motif of Bcl-xL. We replaced this sequence with an engineered E3 containing the TM motif of the ER-based Cytochrome *b*5 (CB5) protein. Cre-recombination induced WT E3 excision and CB5 mutant expression (Figures 1A and 1B). Expression of recombinant ER-Bcl-xL was verified in lung, liver, and brain tissues (Figure 1C). Furthermore, the expected subcellular localization of WT and ER-Bcl-xL was verified in brain tissue using subcellular fractionation (Figures 1D and 1E).

Characterization of the phenotype of ER-xL mice

Though *bclx* KO was reported to lead to embryonic death at E13.5,[8] ER-xL mice survived beyond that stage and were born according to Mendelian rules (Figure S1A). Of interest, ER-xL mice were significantly smaller than WT or heterozygous (HET) littermates (Figures 2A, S1B, and S1C). ER-xL mice lacked visible milk pockets, and when artificially fed, presented incoherent sucking and swallowing reflexes and were unable to survive beyond 24 h (Figures 2A and 2B).

As such behavior might be because of dysfunction of the nervous system, and to further investigate this phenotype, we conducted a histological study focusing on the nervous system using cleaved caspase-3 as a marker of apoptosis. We observed increased caspase-3 signaling in the cortex (Figures 2D and 2G) but also in the hindbrain and the spinal cord (Figure S2).

Of interest, this signal was mainly detected in the white matter, but not the gray matter where the cell bodies of neurons are located, suggesting that the increased caspase-3 signal is not related to apoptosis (Figures 2F, 2G, and S2B–S2E). To test this hypothesis, we isolated and cultured primary cortical neurons for 5 to 7 days (5DIV, 7DIV, see Figure 3A). Under these conditions, we did not observe a higher rate of pyknotic nuclei in neurons from ER-xL mice, compared to WT controls (Figure S3). Of note, the rate of pyknotic nuclei was markedly increased in both WT and ER-XL neurons on treatment with WEHI-539, a specific Bcl-xL inhibitor, indicating that ER-restricted Bcl-xL retains some anti-apoptotic activity (Figure S4).

Of note, staining of WT and ER-xL neurons with active caspase-3 antibody highlighted a positive signal, mostly in the neurites (Figures 3B and S3E). This signal was significantly higher in ER-xL neurons, compared to WT (Figures 3C and 3D).

Analysis of neurite architecture

The above observations raise issues regarding the consequences of this elevated caspase-3 activity and the mechanisms that allow caspase-3 activation in neurites, independent of cell death. Thus, we next investigated the impact of mitochondrial Bcl-xL silencing on axon morphology. We isolated embryonic cortical neurons after electroporation *ex vivo* in the cortex (E15.5) with a Venus-expressing plasmid. Axon morphology was analyzed after 5 days *in vitro* (5DIV). The overall axon length between ER-xL and WT primary neurons was similar (Figure S5A). However, we detected a decrease in axon arborescence in ER-xL neurons, compared to WT (Figures4A, 4B, and S5B). In the course of this study, we also measured the effect of mitochondrial Bcl-xL silencing on dendritic spines, a kind of plastic protrusions that receives pre-synaptic input from neighboring neurons (reviewed by Hering and Sheng[11]). Although the density of dendritic spines was unchanged (Figure S5C), we observed notable changes in their morphology, with a decrease in the number of mushroom-type dendritic spines in ER-xL primary neurons and an increase in filopodial spines (Figures 4C–4E), suggesting that synapse maturation was impacted at the post-synaptic level.

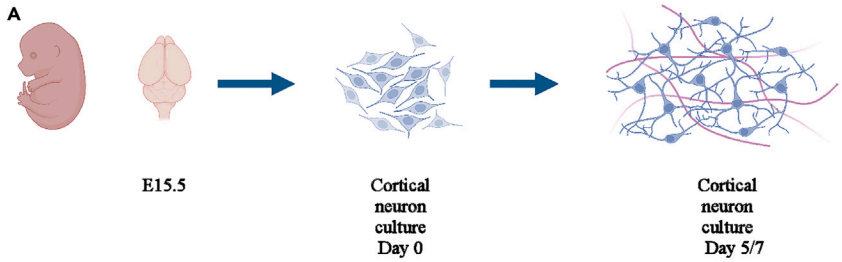
A
E15.5
Cortical neuron culture Day 0
Cortical neuron culture Day 5/7

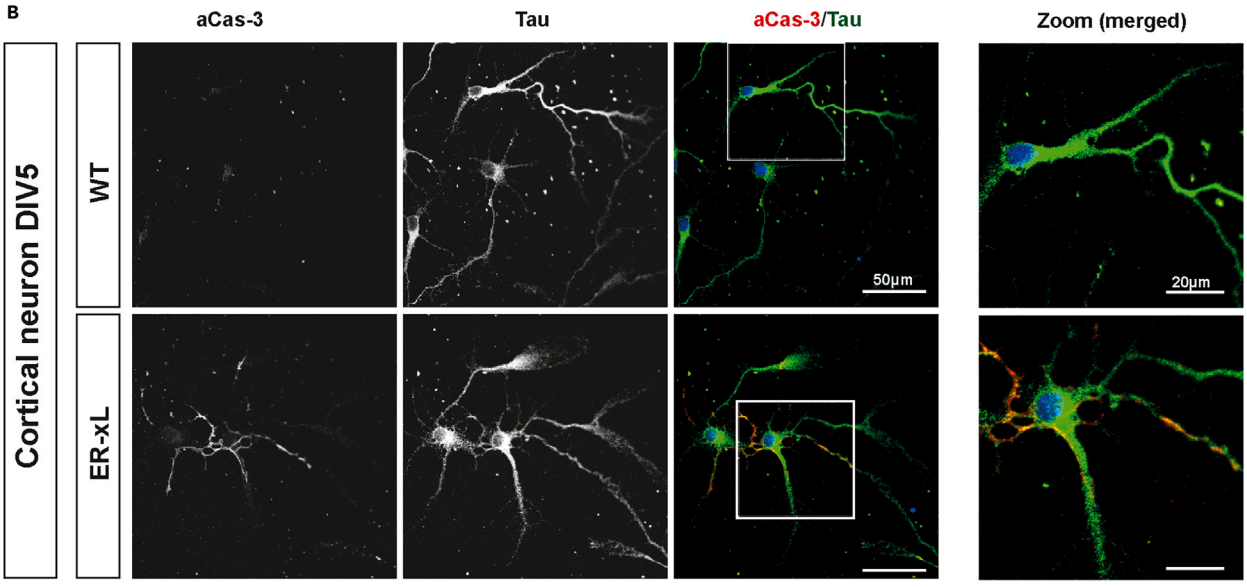
B
aCas-3
Tau
aCas-3/Tau
Zoom (merged)
Cortical neuron DIV5
WT
ER-xL
50µm
20µm

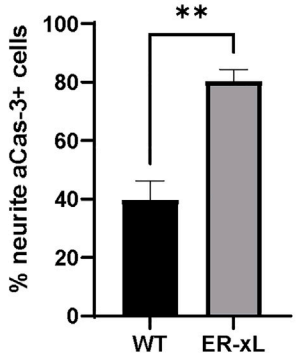
C
% neurite aCas-3+ cells
100
80
60
40
20
0
**
WT
ER-xL

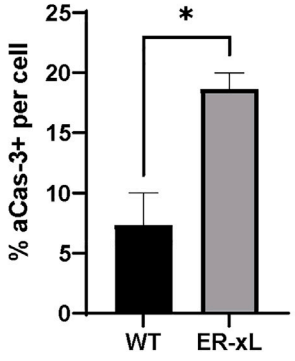
D
% aCas-3+ per cell
25
20
15
10
5
0
*
WT
ER-xL

Figure 3. Loss of mitochondrial Bcl-xL induces caspase-3 activation in the neurites of cortical neurons in culture

(A) Schematic diagram of the cortical neuron isolation procedure. Cortical neurons were isolated from the cerebral cortex of the E15.5 embryo and maintained in culture for 5–7 days *in vitro* (DIV 5–7).

(B) Representative immunofluorescence of WT and ER-xL cortical neurons at DIV7, with active caspase-3 and tau.

(C) Quantification of neurite active caspase-3-positive neurons at DIV7. Data show average value ±SEM from three independent experiments. Student's *t* test was used for statistical analysis: N_{WT} = 37, $N_{ER\text{-}xL}$ = 34.

(D) Quantification of active caspase-3 positive surface per neuron at DIV7. Data show average value ±SEM from three independent experiments. Student's *t* test was used for statistical analysis: N_{WT} = $N_{ER\text{-}xL}$ = 24.*p<0.05; **p<0.01; ***p<0.001.

Finally, to further assess the contribution of caspase-3 to the development of the axon network, we analyzed the effect of the caspase inhibitor Z-DEVD-FMK on the axon morphology of WT and ER-xL neurons. Although Z-DEVD-FMK did not significantly alter WT neuron morphology, it restored both axon arborescence and dendritic spine organization in ER-xL neurons (Figures 4A–4C and 4E). Hence, these observations suggest that the local increase in caspase-3 activity in ER-xL axons drives morphological changes in neurite architecture.

Analysis of synaptogenesis capacities

The above observations suggest that ER-xL mice may display alterations in neural network architecture as a result of deficient synaptogenesis. To assess this hypothesis, we implemented a microfluidic approach to study the pre- and post-synaptic network. In these experiments, neurons were placed in two compartments (referred to as pre- and post-synaptic) connected by microchannels to a synaptic chamber to follow neurite elongation and synapse formation.

First, we seeded both compartments with the same type of neurons (pre-WT/post-WT and pre-ER-xL/post-ER-xL). Active caspase-3 signals could clearly be observed when compartments were seeded with ER-xL but not WT neurons, confirming the results from primary cultures (Figures 5A–5D). Synaptic connections were analyzed with antibodies against synaptophysin and PSD95 used as markers of pre- and post-synaptic compartments of the synapse, respectively. These latter experiments highlighted a deficit in synaptogenesis when performed with ER-xL neurons, compared to WT (Figures 5E and 5F).

Second, synaptogenesis was monitored when compartments were cross-seeded with different cell types (ER-xL or WT). As shown in Figure 6, synaptogenesis was only impacted when ER-xL neurons were present in the pre-synaptic compartment, irrespective of the cell type in the post-synaptic compartment. These findings suggest that defects at the level of axon terminals may be responsible for alterations observed in synaptogenesis.

Analysis of mitochondria dynamics in cortical axons

Activation of effector caspases, depend, although not exclusively, on MOMP. Thus, during apoptosis, activation of the caspase cascade, including downstream caspase-3, follows a decrease in mitochondrial membrane potential ($\Delta\Psi_m$) and the subsequent release of cytochrome *c* into the cytosol. This prompted us to examine the status of mitochondria in ER-xL and WT axons.

We initially measured the $\Delta\Psi_m$ using the tetramethylrhodamine ethyl ester (TMRE). $\Delta\Psi_m$ was significantly lower in the mitochondria of ER-xL axons, compared to that of WT controls (Figure 7A). This decrease was not because of an overall decrease in the area or the number of axon mitochondria (Figures 7B and 7C). However, we found that the level of mitochondrial fragmentation was higher in ER-xL axons, compared to WT (Figures 7D and 7E). In addition, when measuring their velocity we unveiled that mitochondria in ER-xL axons were more motile than mitochondria in WT axons (Figures 7F and 7G). We further used a system composed of two probes, cytoGFP-FKBP and mito-Cherry-FRB, to detect permeabilized mitochondria.[12] Of interest, we observed an increased number of permeabilized mitochondria in ER-xL axons, compared to heterozygous (HET) neurons, suggesting that the enhanced caspase-3 activity may be due to an increase of MOMP in ER-xL axons (Figures 7H and 7I).

Previous studies unveiled Bcl-xL/dynamin-related protein 1 (Drp-1) complexes in neurons.[13,14] The dynamin-like GTPase Drp-1 is recruited to the MOM where it drives mitochondrial fission via GTP-dependent constriction and fosters cytochrome *c* release during apoptosis.[15–17] This prompted us to investigate the interaction between Bcl-xL and Drp-1. We performed co-immunoprecipitation experiments using WT

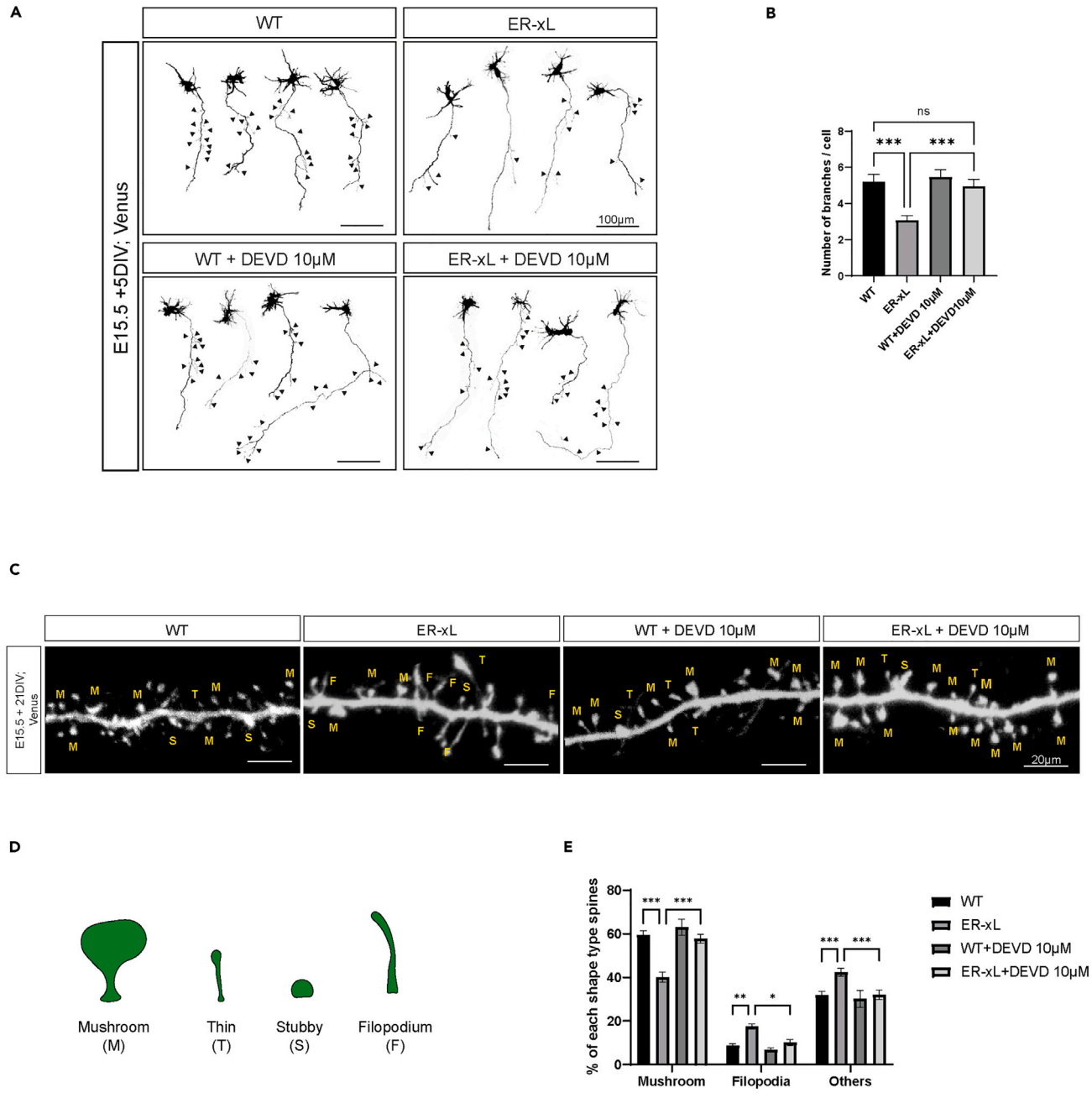

Figure 4. Mitochondrial Bcl-xL is required for axon branching and dendritic spine maturation

(A) Representative images (inverted LUT) of 5DIV neurons from WT and ER-xL cortex without or with treatment with caspase-3 inhibitor Z-DEVD-FMK 10 μM from DIV3. *Ex vivo* cortical electroporation with a Venus-expressing plasmid followed by cortical neuron dissociation was performed at E15.5. Each axonal branch is indicated by an arrowhead.

(B) Histogram showing the effect of the caspase-3 inhibitor Z-DEVD-FMK (10 μM) on the number of axon branches per cell of cortical neurons at DIV5. The treatment with Z-DEVD-FMK was applied from DIV3-5. Data show average value ±SEM from three independent experiments. Kruskal-Wallis test was used for statistical analysis: N_{WT} = 143, $N_{ER\text{-}xL}$ = 140, $N_{WT+DEVD}$ = 122, $N_{ER\text{-}xL+DEVD}$ = 122.

(C) Representative images of dendrites with dendritic spines from DIV21 cortical neurons cultured from the isolated cortex of E15.5 WT and ER-xL embryos without or with the treatment of caspase-3 inhibitor Z-DEVD-FMK 10 μM from DIV14. Neurons were electroporated with Venus to assess their morphology. Representative spine morphology is indicated: M for mushroom, T for thin, S for stubby, and F for Filopodium.

Figure 4. *Continued*

(D) Schematic diagram for four spine morphologies: mushroom, thin, stubby, and filopodium. The mushroom-type spine is defined by a big head and small, short neck morphology, considered the mature form. The filopodial spine has a long, thin shape, considered the immature form.

(E) Histogram showing the effect of caspase-3 inhibitor Z-DEVD-FMK (10 μM) on the spine shape percentage of cortical neurons at DIV21. The treatment with Z-DEVD-FMK was applied from DIV14-21. Data show average value ±SEM from three independent experiments. Two-way ANOVA test was used for statistical analysis: N_{WT} = 22; $N_{ER\text{-}xL}$ = 29; $N_{WT+DEVD}$ = 13; $N_{ER\text{-}xL+DEVD}$ = 23. *p<0.05; **p<0.01; ***p<0.001.

Bcl-xL or ER-addressed Bcl-xL as bait. Compared to native Bcl-xL, ER-Bcl-xL interacted only weakly with Drp-1, suggesting that the Bcl-xL/Drp-1 complex was partly disrupted in ER-xL neurons (Figure 8A). In this respect, it is worth noting that total amounts of Drp-1 were unchanged in ER-xL neurons, compared to WT mice (Figure 8B). To further investigate this finding, we analyzed the effect of the Drp-1 inhibitor *m*-divi on caspase-3 activity in ER-xL axons. As shown in Figures 8C–8E, the caspase-3 signal was suppressed in ER-xL axons, following *m*-divi treatment. Furthermore, expression of the dominant negative Drp1 K38A (dnDrp1) mutant restored the number of axon branches in ER-xL neurons (Figure S6). Collectively, these datas upport the notion that caspase-3 activation in ER-xL axons is Drp-1-dependent and that Bcl-xL controls axon branching by keeping Drp-1 in check.

DISCUSSION

Caspases are a family of intracellular proteases playing an essential role in cell death in metazoans.[18,19] By acting as apoptosis executioners, caspases control the size of cell populations and participate in tissue morphogenesis during embryonic development. However, it is well known that caspase activation is not always associated with apoptosis.[20–23] Moreover, it was recently shown in tumor cells that Bcl-2 inhibitors can trigger NLCA through the permeabilization of a limited number of mitochondria, a process referred to as minority MOMP (miMOMP).[12,24]

Intriguingly, sublethal caspase levels have also been reported to promote neural development processes, including axon branching and synapse formation, but the control of NLCA remains elusive.[22,25,26]

In the present study, we provide evidence that caspase-3 activity and miMOMP are controlled by Bcl-xL in the mouse embryonic brain. Altogether, our data suggest that, during development, the control of NLCA by mitochondrial Bcl-xL is critical for the maturation of the mouse nervous system.

Phenotype of ER-xL individuals

Here, we report that the removal of the mitochondrial pool of Bcl-xL through a KI strategy in mice does not lead to embryonic death as previously described in *bclx* KO mice.[8] ER-xL embryos do not exhibit detectable organ alterations, as shown by histological analyses. Moreover, ER-xL newborns survive up to 24 h with apparent normal mobility. However, these individuals exhibit swallowing defects reminiscent of the 22q11DS syndrome,[27] presumably causing premature death.

A reasonable hypothesis is that the delayed lethality observed in ER-xL individuals compared to *bclx* KO mice (which all die at E13.5) results from a "milder intensity" of cell death. Indeed, in ER-xL embryos (E13.5), an increase in caspase-3 signal in the spinal cord and the brainstem could be detected, but not in the liver. This is in sharp contrast with *bclx* KO mice, where massive apoptotic bodies were reported in the central nervous system (CNS) and the hematopoietic cell population in the liver at the same embryonic stage.[8]

The observed phenotype of ER-xL mice also suggests that the maintenance of the ER pool of Bcl-xL prevents premature embryonic lethality, suggesting that ER-based Bcl-xL plays a protective role in apoptosis. In this regard, treatment of ER-xL neurons with the BH3-mimetic WEHI-539 led to a significant increase in apoptosis, suggesting that the hydrophobic pocket of ER-Bcl-xL is engaged with BH3-only proteins. A non-exclusive possibility is that the anti-apoptotic effect of ER-Bcl-xL would be mediated through ER Ca^{2+} trafficking, as Bcl-xL was shown to control IP3R Ca^{2+} permeability via two BH3-like motifs.[10,28] Furthermore, ER stress, which is closely linked to Ca^{2+} trafficking dysregulation, was reported to contribute to neurogenesis and cortex development.[29–31] It should also be noted that in the *bclx* KO background, a peak of the unfolded protein response (UPR) occurs upstream of embryonic death.[8,32] In this respect, we found that mouse embryonic fibroblasts derived from ER-xL mice are more vulnerable to mitochondrial stress stimuli,

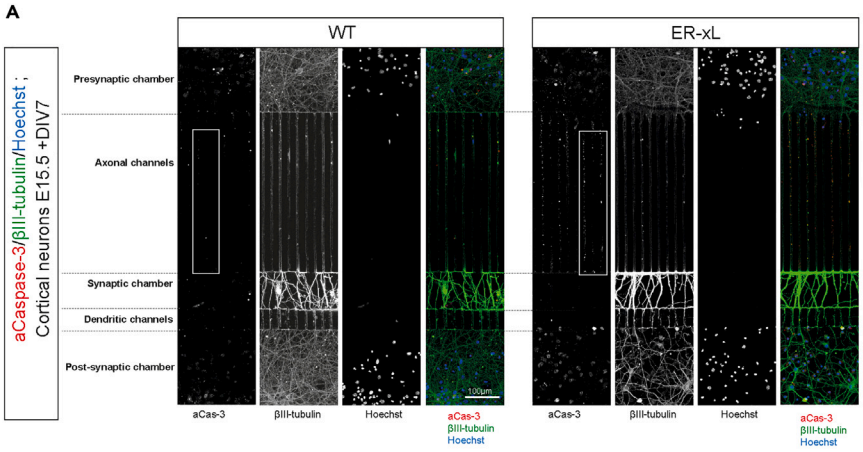
A
WT
ER-xL
aCaspase-3/βIII-tubulin/Hoechst ;
Cortical neurons E15.5 +DIV7
Presynaptic chamber
Axonal channels
Synaptic chamber
Dendritic channels
Post-synaptic chamber
100µm
aCas-3
βIII-tubulin
Hoechst
aCas-3
βIII-tubulin
Hoechst
aCas-3
βIII-tubulin
Hoechst
aCas-3
βIII-tubulin
Hoechst

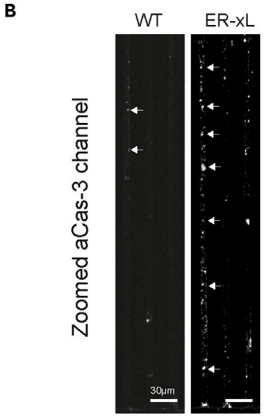
B
WT
ER-xL
Zoomed aCas-3 channel
30µm

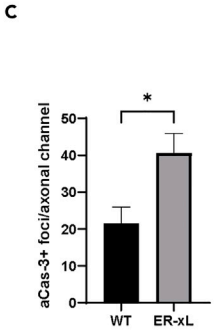
C
aCas-3+ foci/axonal channel
*
50
40
30
20
10
0
WT
ER-xL

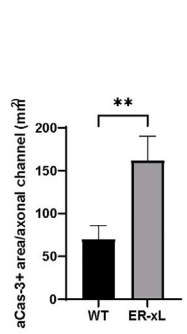
D
aCas-3+ area/axonal channel (mm²)
**
200
150
100
50
0
WT
ER-xL

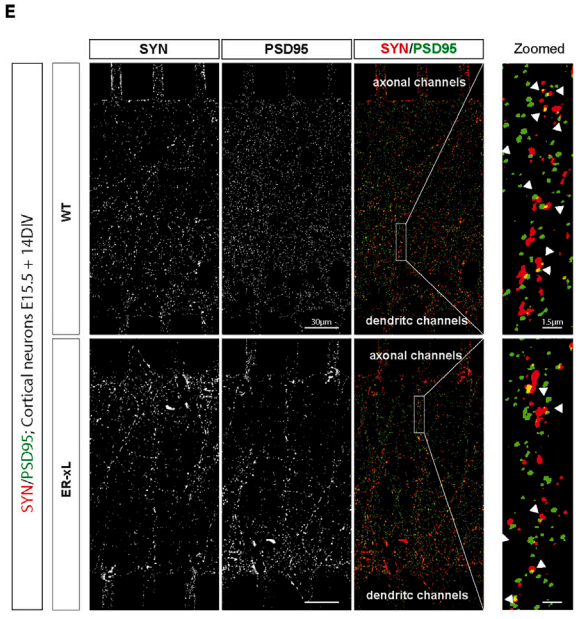
E
SYN
PSD95
SYN/PSD95
Zoomed
SYN/PSD95; Cortical neurons E15.5 + 14DIV
WT
ER-xL
axonal channels
dendritc channels
axonal channels
dendritc channels
30µm
1.5µm

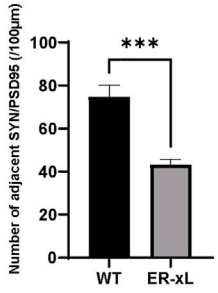
F
Number of adjacent SYN/PSD95 (/100µm)
***
100
80
60
40
20
0
WT
ER-xL

Figure 5. Mitochondrial Bcl-xL regulates synapse formation

(A) Representative immunofluorescence of WT and ER-xL cortical neurons in the 3-compartment microfluidic device with active caspase-3 and βIII-tubulin. Nuclei were marked with Hoechst 33342.

(B) Higher-magnification images of active caspase-3 signals in the axonal channel zone boxed in (A). Arrows point to active caspase-3-positive foci.

(C and D) Quantification of caspase-3-positive foci (E) or area (F) per axon channel at DIV7. Data are from at least three independent experiments. Data show average value ±SEM. Student's *t* test was used for statistical analysis: N_{WT} = 79, $N_{ER\text{-}xL}$ = 84.

(E) Representative immunofluorescence of pre-synaptic protein SYN and post-synaptic protein PSD95 in the synaptic chamber between cortical neurons at 14DIV. Zoomed panels show high magnification images in the zone boxed in the SYN/PSD95 panels. Arrowheads point to adjacent spot SYN/PSD95.

(F) Quantification of adjacent spot SYN/PSD95 per 100 μm of the axon of 14DIV cortical neurons. Data are from at least three independent experiments. Data show average value ±SEM. Student's *t* test was used for statistical analysis: N_{WT} = $N_{ER\text{-}xL}$ = 13.*p<0.05; **p<0.01; ***p<0.001.

but more resistant to ER stress inducers.[33] Thus, ER-localized Bcl-xL is conceivably able to regulate developmental UPR and prevent ER-stress-dependent neuronal cell death during early development.

Caspase-3 activation in ER-xL neurons

Histological analyses revealed that the active caspase-3 signal is higher in the white matter than the gray matter in both the spinal cord and the cortex of ER-xL embryos. Primary cultures of cortical neurons confirmed that such caspase-3 activation was independent of apoptosis. Moreover, microfluidic studies carried out on ER-xL neurons revealed that activated caspase-3 was predominantly found in axons. Together, these data prompted the idea that the marked increase in caspase-3 activity observed in ER-xL neurons may result in neural development abnormalities, leading to premature death shortly after birth.

Impact on axon branching and synaptogenesis

We observed that active caspase-3 *in vitro* can preferentially be found in branching points and contact sites between neurons. We thus hypothesized that aberrant local caspase-3 activation might result in abnormal axon development and synapse formation.

Indeed, morphological analyses performed on ER-xL cortical neurons showed axon branch reduction without any impact on axon length. Treatment with z-DEVD-FMK restored normal axon branching, strongly suggesting that the observed decrease in axon ramifications was because of caspase-3 activation, the contribution of other caspases not being ruled out, given the somewhat relative specificity of z-DEVD-FMK for caspase-3.[34] Paradoxically, transient caspase-3 activation was previously reported to be required for axon branch formation.[35] In the same line, other studies highlighted the role of caspase-3 in axon pruning.[36,37] Here, local caspase-3 activity was also detected at basal levels in WT neurons *in vitro*, which may be critical for major processes such as axon arborization and synapse plasticity.[26,38,39] However, Z-DEVD-FMK did not seem to affect axon arborescence in WT neurons, suggesting that residual caspase activity still ensures branchpoint formation in a WT background. Indeed, contrary to genetic loss-of-function approaches, pharmacological inhibitors may not fully repress caspase activity.[37,40,41]

Collectively, these data suggest that, while baseline caspase-3 activity is critical for the design of axon arborescence, the high levels of caspase-3 activity detected in ER-xL neurons are presumably out of range, resulting in deleterious effects on the generation of axon branches and synaptogenesis.

Impact at the post-synaptic level

Although further investigating synapse maturation by assessing the morphology of dendritic spines, we noticed that ER-xL neurons presented a decreased number of mushroom-like spines, as well as an increased number of filopodia-like spines, suggesting that synapse maturation is impacted at the post-synaptic level. Indeed, caspases have been reported to be present in dendritic spines, presumably contributing to their shaping through cytoskeleton remodeling (reviewed by Mukherjee and Williams[26]). Such mechanisms could actually be compromised in ER-xL neurons. In this regard, it would be worth investigating if Ca^{2+} trafficking, which is also known to contribute to cytoskeleton dynamics, is affected in the ER-xL background.

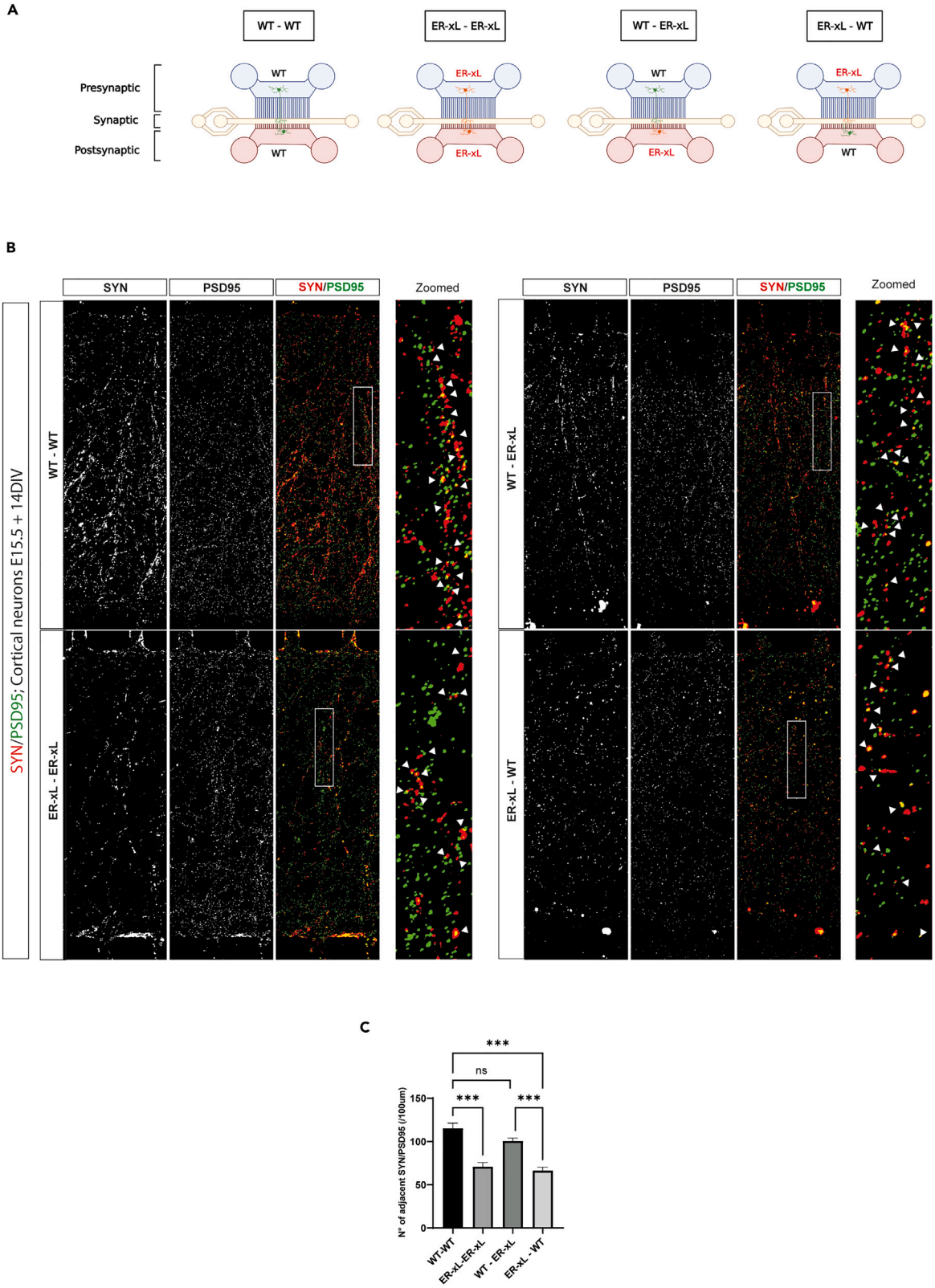
A
WT - WT
ER-xL - ER-xL
WT - ER-xL
ER-xL - WT
Presynaptic
Synaptic
Postsynaptic
WT
ER-xL
B
SYN
PSD95
SYN/PSD95
Zoomed
SYN/PSD95; Cortical neurons E15.5 + 14DIV
WT - WT
ER-xL - ER-xL
WT - ER-xL
ER-xL - WT
C
N° of adjacent SYN/PSD95 (/100um)
150
100
50
0
***
ns
***
***
WT-WT
ER-xL-ER-xL
WT - ER-xL
ER-xL - WT

Figure 6. Mitochondrial Bcl-xL regulates synaptogenesis at pre-synaptic sites

(A) Schematic diagram of strategy for manipulating the genetic status of pre-synaptic and post-synaptic neurons. Four combinations were tested: WT - WT, ER-xL – ER-xL, WT – ER-xL, and ER-xL – WT.

(B) Representative immunofluorescence of pre-synaptic protein SYN and post-synaptic protein PSD95 in the synaptic chamber between cortical neurons at 14DIV of WT – WT, ER-xL – ER-xL, WT – ER-xL, and ER-xL – WT. Zoomed panels show high magnification images in the zone boxed in the Syn/PSD95 panels. Arrowheads point to adjacent spot SYN/PSD95.

(C) Quantification of adjacent spot SYN/PSD95 per 100 μm of axon of 14DIV cortical neurons. Data are from three independent experiments. Data show average value ±SEM. Kruskal-Wallis test was used for statistical analyses. $N_{WT\text{-}WT}$ =54, $N_{ER\text{-}xL\text{-}ER\text{-}xL}$ = 50, $N_{WT\text{-}ER\text{-}xL}$ = 51, $N_{ER\text{-}xL\text{-}WT}$ = 49.*p<0.05; **p<0.01; ***p<0.001.

Impact at the pre-synaptic level

Together our data suggest that ER-xL neurons exhibit abnormalities in synapse formation and maturation, as illustrated by alterations in dendritic spine morphology. Our microfluidic analyses suggest that these synaptic alterations may also depend on pre-synaptic events.

Indeed, these latter analyses confirmed that synaptogenesis is altered in the ER-xL background, as shown by monitoring synaptophysin and PSD95 vicinity. Of note, the seeding of WT neurons, but not ER-xL neurons, in the pre-synaptic compartment ensures synaptophysin and PSD95 juxtaposition, irrespective of post-synaptic cell genetic background (ER-xL or WT). This observation suggests that pre-synaptic signals emitted by the growing axon are defective in the ER-xL background, compromising synaptogenesis. Bcl-xL was reported to contribute to vesicle trafficking and promote ATP generation in nerve cells.[14,42] Such mechanisms may be impacted in ER-xL neurons, notably through enhanced caspase activity,[43] leading to axonal termination dysfunction.

It remains to be investigated if synapses formed between a WT pre-synaptic moiety and an ER-xL post-synaptic moiety are fully functional. Indeed, the dynamics of the actin cytoskeleton at the post-synaptic level is presumably still deficient, with deleterious consequences on dendritic spine maturation to be expected.[26,43]

Mitochondrial status

Our data also indicate that the status of mitochondria is altered in axons from cortical ER-xL neurons with changes reminiscent of apoptosis, such as increased fragmentation and drop of $\Delta\Psi m$, together with increased motility. The Bax/Bad/Caspase-3 cascade is presumably activated to some extent (although at a sublethal level) as a consequence of these mitochondrial changes, contributing to the observed defects in synaptogenesis. In addition, co-immunoprecipitation experiments suggest that BclxL/Drp-1 interactions are compromised in the ER-xL background. In this latter context, the presumed partial activation of Bax, with Bcl-xL absent from mitochondria, would increase the mitochondrial fission/fusion ratio. Indeed, Bax activation might both decrease mitofusin activity, thus reducing the rate of fusion,[44] and increase Drp-1/Bax interactions, thus promoting fission.[45,46] The fact that the Drp-1 inhibitor *m*-divi, despite its debated specificity,[47] and the dominant negative Drp-1 mutant respectively dampen caspase-3 activation, and restore axon arborescence in ER-xL neurons, provides additional evidence about this presumptive role for Drp-1 in the ER-xL background.

Of interest, Bcl-xL was reported to foster Drp-1 GTPase activity, facilitating synaptic vesicle turnover and synaptic transmission.[13,14] Evidence indicates that Bcl-xL promotes mitochondrial dynamics by acting on both mitochondrial fission and fusion, thereby supplying ATP to energy-demanding processes at the pre- and post-synaptic levels.[48]

At the mitochondrial level, our data support the idea that, in addition to promoting ATP supply, Bcl-xL is able to limit the formation of active Drp-1/Bax complexes, probably in part through inhibition of Bax, and thus prevent excess mitochondrial fission (see e.g., Maes et al.[45]; Jenner et al.[46]), which might be deleterious. Thus our observations provide an additional layer of complexity, indicating that Bcl-xL might either positively or negatively control Drp-1, depending on its localization and partners. In this respect, it would be worth determining the post-translational modifications of Drp-1 and their role in the control of Drp-1 activity in our model.[49]

The observed mitochondria-dependent activation of caspase-3 in the ER-xL background is likely to be strictly controlled over time and space because it is limited to the neurites without detectable apoptosis.

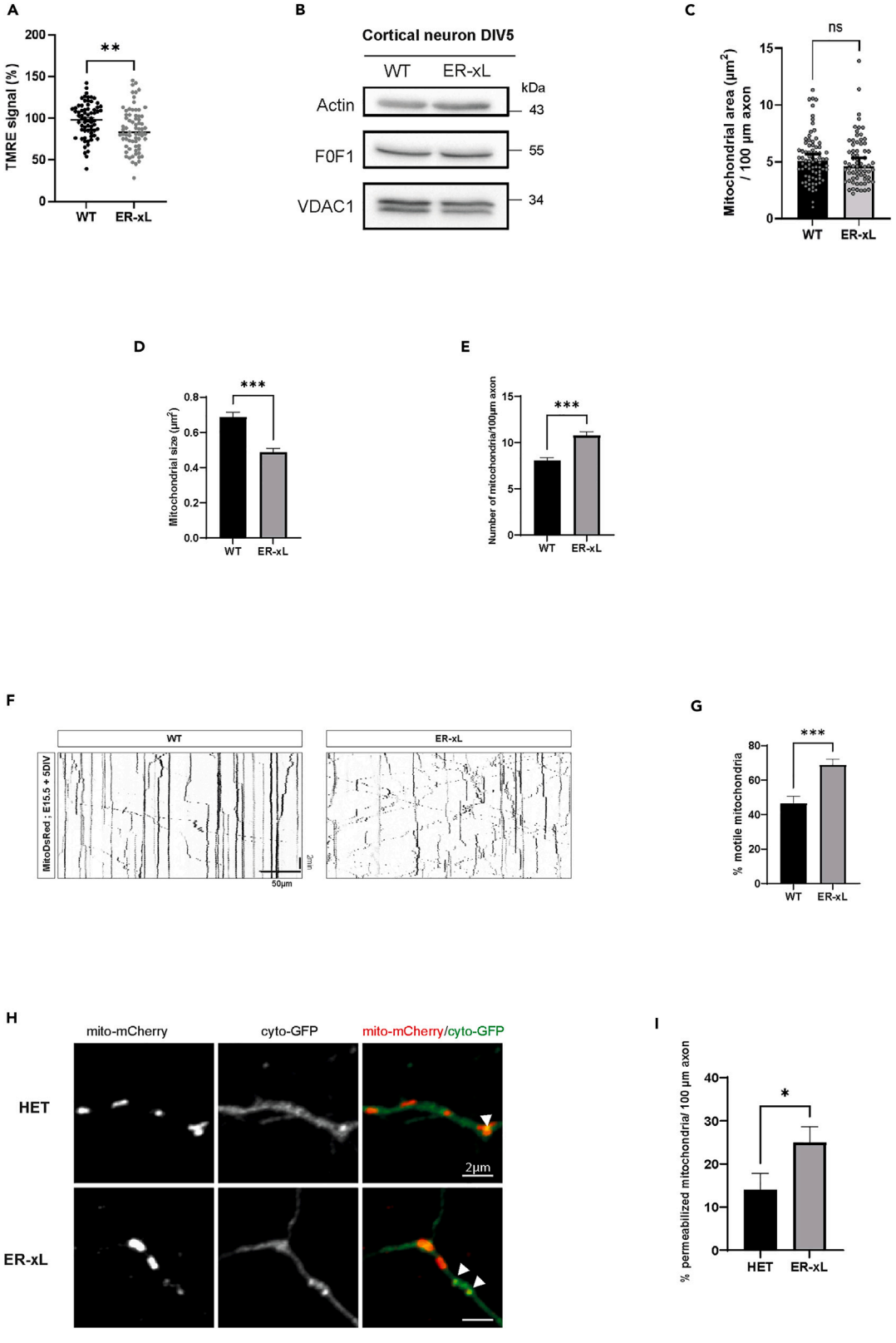
A
TMRE signal (%)
200
150
100
50
0
**
WT
ER-xL
B
Cortical neuron DIV5
WT
ER-xL
kDa
Actin
43
F0F1
55
VDAC1
34
C
Mitochondrial area (µm²) / 100 µm axon
ns
15
10
5
0
WT
ER-xL
D
Mitochondrial size (µm²)
***
0.8
0.6
0.4
0.2
0.0
WT
ER-xL
E
Number of mitochondria/100µm axon
***
15
10
5
0
WT
ER-xL
F
WT
ER-xL
MitoDsRed ; E15.5 + 5DIV
2min
50µm
G
% motile mitochondria
***
80
60
40
20
0
WT
ER-xL
H
mito-mCherry
cyto-GFP
mito-mCherry/cyto-GFP
HET
ER-xL
2µm
I
% permeabilized mitochondria/ 100 µm axon
*
40
30
20
10
0
HET
ER-xL

Figure 7. Loss of mitochondrial Bcl-xL induces changes in axonal mitochondrial morphology, dynamics, and potential

(A) Quantification of mitochondrial membrane potential by TMRE of axonal mitochondria in WT and ER-xL neurons at DIV5. Each point represents the average value for a given neuron Datashow average value ±SEM from three independent experiments. Student's *t* test was used for statistical analysis. N_{WT} = 68, $N_{ER\text{-}xL}$ = 71.

(B) Expression of mitochondrial proteins in neurons at DIV5 derived from the cortex of WT and ER-xL E15.5 cerebral cortices. Western blot analysis was performed with indicated antibodies. Actin was used as the loading control.

(C–E) Quantification of area occupied by mitochondria per 100 μm of the axon (C), mitochondria size (D), and number of mitochondria per 100 μm axon (E) of the cortical neuron at DIV5. Neurons were electroporated at E15.5 by electroporation *ex vivo* with Venus to mark the axon and mitoDsRed to label mitochondria. Data show average values ±SEM. Data are from three independent experiments. Mann-Whitney test was used for statistical analysis. N_{WT} = 79, $N_{ER\text{-}xL}$ = 69.

(F) Representative kymographs of axonal mitochondria in dissociated cortical neurons at DIV5. Neurons were electroporated with MitoDsRed and mVenus.

(G) Quantification of motile axonal mitochondria. Data show average values ±SEM. Data are from three independent experiments. Student's *t* test was used for statistical analysis. N_{WT} = 19, $N_{ER\text{-}xL}$ = 20. (H) Representative image of miMOMP in the axon of HET and ER-xL cortical neurons. Permeabilization of individual mitochondrion was detected by colocalization of mito-mCherry-FRB (targeted to the mitochondrial inner membrane (MIM) by Apoptosis Inducing Factor (AIF) sequence) and cyto-GFP-FKBP. When a mitochondrion is permeabilized, cyto-GFP-FKBP freely accesses the mitochondrial inner membrane and can dimerize with mito-mCherry-FRB in the presence of a dimerization inducer. Cortical neurons were electroporated with vectors containing mito-mCherry-FRB and cyto-GFP-FKBP. After 7 days in culture, neurons were treated with the A/C heterodimerizer for 1 h to induce the dimerization between FRB and FKBP and imaged by confocal microscopy using Airyscan. Arrowhead points to the permeabilized mitochondrion, which is detected by the colocalization between mito-mCherry and cyto-GFP signals.

(I) Quantification of permeabilized mitochondria in the axon of cortical neurons. Data are from three different embryos. Datashow average value ±SEM. Mann-Whitney test was used for statistical analysis: N_{WT} = 15; $N_{ER\text{-}xL}$ = 14*p<0.05; **p<0.01; ***p<0.001.

Consistently, the contribution of ER-Bcl-xL might be critical to prevent deleterious cell death. Finally, our observations regarding increased fragmentation and permeabilization of mitochondria in ER-xl axons are reminiscent of miMOMP and subsequent sublethal caspase-3 activation as recently described in cancer cells.[50] Indeed, in ER-xl axons, mitochondria might be similarly primed to death, promoting caspase-3 activation with consequences on axon arborescence and synaptogenesis.

Overall, our data support the idea that Bcl-xL, controls miMOMP and acts on the mitochondrial network dynamics in axons. We provide evidence that, in this way, Bcl-xL fosters axon branching and synaptogenesis (see diagram in Figure 9). Although several issues remain to be addressed, in particular figuring out why mitochondria are not impacted in the soma of ER-xL neurons, the mouse model described in the present report sheds new light on the role of Bcl-2 family proteins in the developing CNS and may open novel avenues regarding neurodegenerative diseases.

Limitations of the study

Several issues remain to be addressed, including:

- *why ER-xl mice die prematurely?* We provide evidence that the individuals suffer from swallowing defects reminiscent of the 22q11DS syndrome, however the exact brain area and nerve pathways that are affected remain to be determined.
- *why mitochondria are not impacted in the soma of ER-xL neurons*? The status of the death accelerator Bax and the contribution of the endoplasmic reticulum are unknown.
- *what are the impacted underlying molecular mechanisms?* In this model, we observe that suppression of Mito-Bcl-xL results in increased caspase-3 activity, which presumably impacts a number of processes, including endocytosis, cytoskeleton remodeling, metabolism and electrical activity. The description of the impacted pathways remains to be carried out.

STAR★METHODS

Detailed methods are provided in the online version of this paper and include the following:

- KEY RESOURCES TABLE
- RESOURCE AVAILABILITY
  - Lead contact
  - Materials availability
  - Data and code availability
- EXPERIMENTAL MODEL AND SUBJECT DETAILS
- METHOD DETAILS

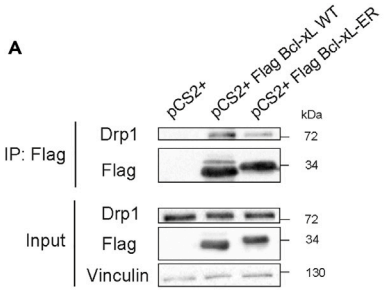
A
pCS2+
pCS2+ Flag Bcl-xL WT
pCS2+ Flag Bcl-xL-ER
kDa
IP: Flag
Drp1
Flag
72
34
Input
Drp1
Flag
Vinculin
72
34
130

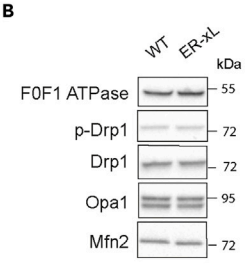
B
WT
ER-xL
kDa
F0F1 ATPase
p-Drp1
Drp1
Opa1
Mfn2
55
72
72
95
72

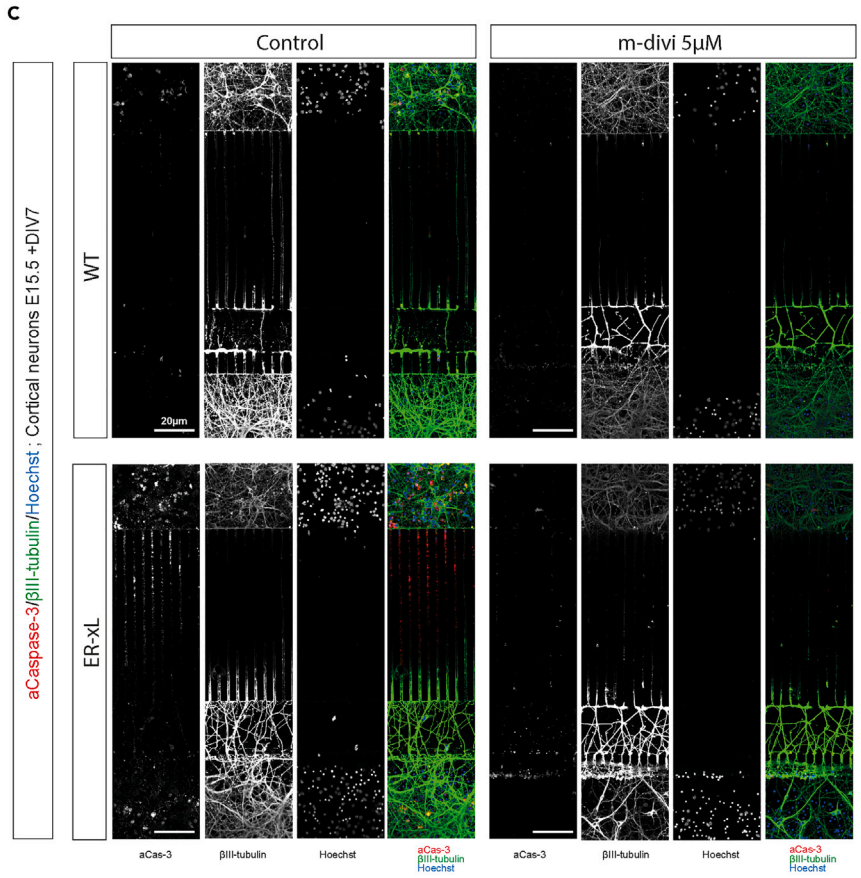
C
Control
m-divi 5µM
aCaspase-3/βIII-tubulin/Hoechst ; Cortical neurons E15.5 +DIV7
WT
ER-xL
20µm
aCas-3
βIII-tubulin
Hoechst
aCas-3
βIII-tubulin
Hoechst

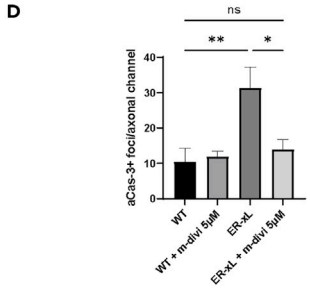
D
ns
**
*
aCas-3+ foci/axonal channel
0
10
20
30
40
WT
WT + m-divi 5µM
ER-xL
ER-xL + m-divi 5µM

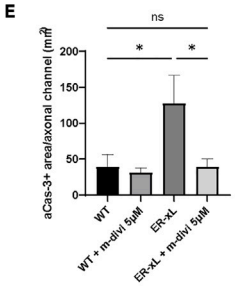
E
ns
*
*
aCas-3+ area/axonal channel (mm²)
0
50
100
150
200
WT
WT + m-divi 5µM
ER-xL
ER-xL + m-divi 5µM

Figure 8. Mitochondrial Bcl-xL regulates axonal local caspase-3 activation via Drp-1

(A) Immunoblot analysis of co-immunoprecipitation between Flag-tagged Bcl-xL WT and Bcl-xL-ER with Drp-1 in HeLa cells.
(B) Expression of mitochondrial fusion and fission proteins in the cortical neurons at 7DIV. Western blot analysis was performed with indicated antibodies. F0F1 ATPase is used as the loading control.
(C) Representative images of cortical neurons in the microfluidic device at 7DIV: WT without treatment (control), WT with *m*-divi 5 μM from 5DIV, ER-xL without treatment, (control) and ER-xL with *m*-divi 5 μM from 5DIV.
(D and E) Quantification of caspase-3-positive foci (D) or area (E) per axon channel at DIV7. Data are from three independent experiments. Data show average value ± SEM. ANOVA test was used for statistical analysis. $N_{WT} = N_{WT+m\text{-}divi} = N_{ER\text{-}xL+m\text{-}divi} = 7$, $N_{ER\text{-}xL} = 6$.*$p < 0.05$; **$p < 0.01$; ***$p < 0.001$.

- *Ex vivo* electroporation
- Primary cortical neuron culture
- Microfluidic chamber preparation
- Western blotting
- Co-immunoprecipitation
- Subcellular fractionation
- TMRE labeling
- Immunofluorescence
- Immunohistochemistry
- Mitochondrial permeabilization detection
- Image acquisition and analysis

- QUANTIFICATION AND STATISTICAL ANALYSIS

SUPPLEMENTAL INFORMATION

Supplemental information can be found online at https://doi.org/10.1016/j.isci.2023.106674.

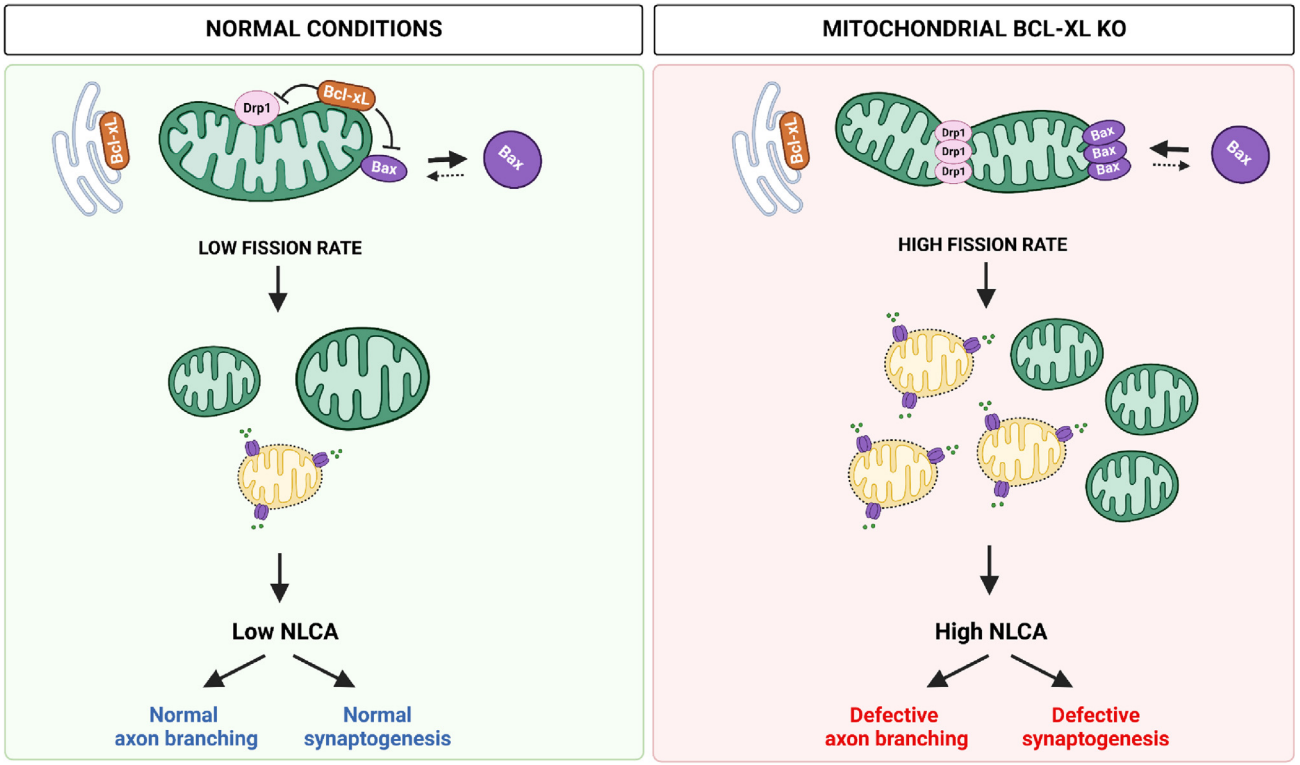

Figure 9. Proposed model for the role of mitochondrial pool of Bcl-xL in the developing axon

Bcl-xL has a dual cellular localization: ER and mitochondrial. In normal condition (left panel), mitochondrial Bcl-xL regulates non-lethal caspase activation (NLCA) in the developing axon through: 1/preventing mitochondrial Bax accumulation via retro-translocation and 2/regulating Drp-1-regulated mitochondrial fission. These activities confine caspase activation in the range that promotes neuronal development. Mitochondrial Bcl-xL lack, whereas its ER pool is maintained, leads to increase of caspase activation perturbing axon branching and synaptogenesis (right panel).

ACKNOWLEDGMENTS

We wish to thank Gabriel Ichim for critical reading of the manuscript. We acknowledge Arnaud Jacquier and the staff of the "Ciqle" imaging facility at "SFR-Santé-Lyon Est" for skillful technical support. TTMN was a fellow from foundation ARC. This work was funded by AFM (grant # 20269 to GG).

AUTHOR CONTRIBUTIONS

T.T.M.N. performed the experiments and wrote the manuscript.

M.L. and S.Y. contributed to the experiments with primary neurons.

R.A.L. contributed to microfluidics experiments.

R.G. performed biochemistry, cell biology, and histology experiments.

O.L. was in charge of mice management and mouse fibroblasts handling.

I.M. designed the mouse model.

L.J. performed western blotting experiments.

R.R. supervised histology experiments.

J.C. supervised and financed the experiments related to the use of primary neurons.

F.S. supervised and financed the experiments related to the use of microfluidic devices, read and corrected the ms.

N.P. supervised the research and wrote the manuscript.

G.G. supervised and financed the research and wrote the manuscript.

DECLARATION OF INTERESTS

The authors declare no conflict of interest.

Received: October 28, 2022
Revised: January 25, 2023
Accepted: April 11, 2023
Published: April 14, 2023

REFERENCES

1. Gross, A., McDonnell, J.M., and Korsmeyer, S.J. (1999). BCL-2 family members and the mitochondria in apoptosis. Genes Dev. *13*, 1899–1911.

2. Chipuk, J.E., Moldoveanu, T., Llambi, F., Parsons, M.J., and Green, D.R. (2010). The BCL-2 family reunion. Mol. Cell *37*, 299–310. https://doi.org/10.1016/j.molcel.2010.01.025.

3. Mattson, M.P. (2000). Apoptosis in neurodegenerative disorders. Nat. Rev. Mol. Cell Biol. *1*, 120–129. https://doi.org/10.1038/35040009.

4. Delbridge, A.R.D., Grabow, S., Strasser, A., and Vaux, D.L. (2016). Thirty years of BCL-2: translating cell death discoveries into novel cancer therapies. Nat. Rev. Cancer *16*, 99–109. https://doi.org/10.1038/nrc.2015.17.

5. Opferman, J.T., and Kothari, A. (2018). Anti-apoptotic BCL-2 family members in development. Cell Death Differ. *25*, 37–45. https://doi.org/10.1038/cdd.2017.170.

6. González-García, M., García, I., Ding, L., O'Shea, S., Boise, L.H., Thompson, C.B., and Núñez, G. (1995). bcl-x is expressed in embryonic and postnatal neural tissues and functions to prevent neuronal cell death. Proc. Natl. Acad. Sci. USA *92*, 4304–4308.

7. Lindsten, T., Zong, W.-X., and Thompson, C.B. (2005). Defining the role of the bcl-2 family of proteins in the nervous system. Neuroscientist *11*, 10–15. https://doi.org/10.1177/1073858404269267.

8. Motoyama, N., Wang, F., Roth, K.A., Sawa, H., Nakayama, K., Nakayama, K., Negishi, I., Senju, S., Zhang, Q., Fujii, S., et al. (1995). Massive cell death of immature hematopoietic cells and neurons in Bcl-x-deficient mice. Science *267*, 1506–1510. https://doi.org/10.1126/science.7878471.

9. Morris, J.L., Gillet, G., Prudent, J., and Popgeorgiev, N. (2021). Bcl-2 family of proteins in the control of mitochondrial calcium signalling: an old chap with new roles. Int. J. Mol. Sci. *22*, 3730. https://doi.org/10.3390/ijms22073730.

10. Rosa, N., Ivanova, H., Wagner, L.E., Kale, J., La Rovere, R., Welkenhuyzen, K., Louros, N., Karamanou, S., Shabardina, V., Lemmens, I., et al. (2022). Bcl-xL acts as an inhibitor of IP3R channels, thereby antagonizing Ca2+-driven

apoptosis. Cell Death Differ. *29*, 788–805. https://doi.org/10.1038/s41418-021-00894-w.

11. Hering, H., and Sheng, M. (2001). Dentritic spines : structure, dynamics and regulation. Nat. Rev. Neurosci. *2*, 880–888. https://doi.org/10.1038/35104061.

12. Ichim, G., Lopez, J., Ahmed, S.U., Muthalagu, N., Giampazolias, E., Delgado, M.E., Haller, M., Riley, J.S., Mason, S.M., Athineos, D., et al. (2015). Limited mitochondrial permeabilization causes DNA damage and genomic instability in the absence of cell death. Mol. Cell *57*, 860–872. https://doi.org/10.1016/j.molcel.2015.01.018.

13. Li, H., Chen, Y., Jones, A.F., Sanger, R.H., Collis, L.P., Flannery, R., McNay, E.C., Yu, T., Schwarzenbacher, R., Bossy, B., et al. (2008). Bcl-xL induces Drp1-dependent synapse formation in cultured hippocampal neurons. Proc. Natl. Acad. Sci. USA *105*, 2169–2174. https://doi.org/10.1073/pnas.0711647105.

14. Li, H., Alavian, K.N., Lazrove, E., Mehta, N., Jones, A., Zhang, P., Licznerski, P., Graham, M., Uo, T., Guo, J., et al. (2013). A Bcl-xL-Drp1 complex regulates synaptic vesicle membrane dynamics during endocytosis. Nat. Cell Biol. *15*, 773–785. https://doi.org/10.1038/ncb2791.

15. Estaquier, J., and Arnoult, D. (2007). Inhibiting Drp1-mediated mitochondrial fission selectively prevents the release of cytochrome c during apoptosis. Cell Death Differ. *14*, 1086–1094. https://doi.org/10.1038/sj.cdd.4402107.

16. Prudent, J., Zunino, R., Sugiura, A., Mattie, S., Shore, G.C., and McBride, H.M. (2015). MAPL SUMOylation of Drp1 stabilizes an ER/mitochondrial platform required for cell death. Mol. Cell *59*, 941–955. https://doi.org/10.1016/j.molcel.2015.08.001.

17. Banerjee, R., Mukherjee, A., and Nagotu, S. (2022). Mitochondrial dynamics and its impact on human health and diseases: inside the DRP1 blackbox. J. Mol. Med. (Limerick) *100*, 1–21. https://doi.org/10.1007/s00109-021-02150-7.

18. Wolf, B.B., and Green, D.R. (1999). Suicidal tendencies: apoptotic cell death by caspase family proteinases. J. Biol. Chem. *274*, 20049–20052. https://doi.org/10.1074/jbc.274.29.20049.

19. Van Opdenbosch, N., and Lamkanfi, M. (2019). Caspases in cell death, inflammation, and disease. Immunity *50*, 1352–1364. https://doi.org/10.1016/j.immuni.2019.05.020.

20. Ishizaki, Y., Jacobson, M.D., and Raff, M.C. (1998). A role for caspases in lens fiber differentiation. J. Cell Biol. *140*, 153–158.

21. De Maria, R., Zeuner, A., Eramo, A., Domenichelli, C., Bonci, D., Grignani, F., Srinivasula, S.M., Alnemri, E.S., Testa, U., and Peschle, C. (1999). Negative regulation of erythropoiesis by caspase-mediated cleavage of GATA-1. Nature *401*, 489–493. https://doi.org/10.1038/46809.

22. D'Amelio, M., Cavallucci, V., and Cecconi, F. (2010). Neuronal caspase-3 signaling: not only cell death. Cell Death Differ. *17*, 1104–1114. https://doi.org/10.1038/cdd.2009.180.

23. Brokatzky, D., Dörflinger, B., Haimovici, A., Weber, A., Kirschnek, S., Vier, J., Metz, A., Henschel, J., Steinfeldt, T., Gentle, I.E., and Häcker, G. (2019). A non-death function of the mitochondrial apoptosis apparatus in immunity. EMBO J. *38*, e100907. https://doi.org/10.15252/embj.2018100907.

24. Berthenet, K., Castillo Ferrer, C., Fanfone, D., Popgeorgiev, N., Neves, D., Bertolino, P., Gibert, B., Hernandez-Vargas, H., and Ichim, G. (2020). Failed apoptosis enhances melanoma cancer cell aggressiveness. Cell Rep. *31*, 107731. https://doi.org/10.1016/j.celrep.2020.107731.

25. Unsain, N., and Barker, P.A. (2015). New views on the misconstrued: executioner caspases and their diverse non-apoptotic roles. Neuron *88*, 461–474. https://doi.org/10.1016/j.neuron.2015.08.029.

26. Mukherjee, A., and Williams, D.W. (2017). More alive than dead: non-apoptotic roles for caspases in neuronal development, plasticity and disease. Cell Death Differ. *24*, 1411–1421. https://doi.org/10.1038/cdd.2017.64.

27. Welby, L., Caudill, H., Yitsege, G., Hamad, A., Bunyak, F., Zohn, I.E., Maynard, T., LaMantia, A.-S., Mendelowitz, D., and Lever, T.E. (2020). Persistent feeding and swallowing deficits in a mouse model of 22q11.2 deletion syndrome. Front. Neurol. *11*, 4. https://doi.org/10.3389/fneur.2020.00004.

28. Yang, J., Vais, H., Gu, W., and Foskett, J.K. (2016). Biphasic regulation of InsP3 receptor gating by dual Ca2+ release channel BH3-like domains mediates Bcl-xL control of cell viability. Proc. Natl. Acad. Sci. USA *113*, E1953–E1962. https://doi.org/10.1073/pnas.1517935113.

29. Mimura, N., Yuasa, S., Soma, M., Jin, H., Kimura, K., Goto, S., Koseki, H., and Aoe, T. (2008). Altered quality control in the endoplasmic reticulum causes cortical dysplasia in knock-in mice expressing a mutant BiP. Mol. Cell Biol. *28*, 293–301. https://doi.org/10.1128/MCB.00473-07.

30. Cho, Y.M., Jang, Y.-S., Jang, Y.-M., Chung, S.-M., Kim, H.-S., Lee, J.-H., Jeong, S.-W., Kim, I.-K., Kim, J.J., Kim, K.-S., and Kwon, O.J. (2009). Induction of unfolded protein response during neuronal induction of rat bone marrow stromal cells and mouse embryonic stem cells. Exp. Mol. Med. *41*, 440–452. https://doi.org/10.3858/emm.2009.41.6.049.

31. Laguesse, S., Creppe, C., Nedialkova, D.D., Prévot, P.P., Borgs, L., Huysseune, S., Franco, B., Duysens, G., Krusy, N., Lee, G., et al. (2015). A dynamic unfolded protein response contributes to the control of cortical neurogenesis. Dev. Cell *35*, 553–567. https://doi.org/10.1016/j.devcel.2015.11.005.

32. Frank, C.L., Ge, X., Xie, Z., Zhou, Y., and Tsai, L.-H. (2010). Control of activating transcription factor 4 (ATF4) persistence by multisite phosphorylation impacts cell cycle progression and neurogenesis. J. Biol. Chem. *285*, 33324–33337. https://doi.org/10.1074/jbc.M110.140699.

33. Jabbour, L., Nguyen, T., Gadet, R., Lohez, O., Mikaelian, I., Gonzalo, P., Luyten, T., Chalabi-Dcha, M., Bultynck, G., Rimokh, R., et al. (2021). The endoplasmic reticulum pool of Bcl-xL dampens the unfolded protein response through IP3R-dependent calcium release. Preprint at bioRxiv. https://doi.org/10.1101/2021.01.27.428229.

34. Garcia-Calvo, M., Peterson, E.P., Leiting, B., Ruel, R., Nicholson, D.W., and Thornberry, N.A. (1998). Inhibition of human caspases by peptide-based and macromolecular inhibitors. J. Biol. Chem. *273*, 32608–32613. https://doi.org/10.1074/jbc.273.49.32608.

35. Campbell, D.S., and Okamoto, H. (2013). Local caspase activation interacts with Slit-Robo signaling to restrict axonal arborization. J. Cell Biol. *203*, 657–672. https://doi.org/10.1083/jcb.201303072.

36. Nikolaev, A., McLaughlin, T., O'Leary, D.D.M., and Tessier-Lavigne, M. (2009). APP binds DR6 to trigger axon pruning and neuron death via distinct caspases. Nature *457*, 981–989. https://doi.org/10.1038/nature07767.

37. Cusack, C.L., Swahari, V., Hampton Henley, W., Michael Ramsey, J., and Deshmukh, M. (2013). Distinct pathways mediate axon degeneration during apoptosis and axon-specific pruning. Nat. Commun. *4*, 1876. https://doi.org/10.1038/ncomms2910.

38. Hollville, E., and Deshmukh, M. (2018). Physiological functions of non-apoptotic caspase activity in the nervous system. Semin. Cell Dev. Biol. *82*, 127–136. https://doi.org/10.1016/j.semcdb.2017.11.037.

39. Gu, Q., Jiao, S., Duan, K., Wang, Y.-X., Petralia, R.S., and Li, Z. (2021). The BAD-BAX-caspase-3 cascade modulates synaptic vesicle pools via autophagy. J. Neurosci. *41*, 1174–1190. https://doi.org/10.1523/JNEUROSCI.0969-20.2020.

40. Simon, D.J., Weimer, R.M., McLaughlin, T., Kallop, D., Stanger, K., Yang, J., O'Leary, D.D.M., Hannoush, R.N., and Tessier-Lavigne, M. (2012). A caspase cascade regulating developmental axon degeneration. J. Neurosci. *32*, 17540–17553. https://doi.org/10.1523/JNEUROSCI.3012-12.2012.

41. Unsain, N., Higgins, J.M., Parker, K.N., Johnstone, A.D., and Barker, P.A. (2013). XIAP regulates caspase activity in degenerating axons. Cell Rep. *4*, 751–763. https://doi.org/10.1016/j.celrep.2013.07.015.

42. Alavian, K.N., Li, H., Collis, L., Bonanni, L., Zeng, L., Sacchetti, S., Lazrove, E., Nabili, P., Flaherty, B., Graham, M., et al. (2011). Bcl-xL regulates metabolic efficiency of neurons through interaction with the mitochondrial F1FO ATP synthase. Nat. Cell Biol. *13*, 1224–1233. https://doi.org/10.1038/ncb2330.

43. Duclos, C.M., Champagne, A., Carrier, J.C., Saucier, C., Lavoie, C.L., and Denault, J.-B. (2017). Caspases play in traffic. Cell Death Dis.

8, e2636. https://doi.org/10.1038/cddis.2017.55.

44. Hoppins, S., Edlich, F., Cleland, M.M., Banerjee, S., McCaffery, J.M., Youle, R.J., and Nunnari, J. (2011). The soluble form of Bax regulates mitochondrial fusion via MFN2 homotypic complexes. Mol. Cell *41*, 150–160. https://doi.org/10.1016/j.molcel.2010.11.030.

45. Maes, M.E., Grosser, J.A., Fehrman, R.L., Schlamp, C.L., and Nickells, R.W. (2019). Completion of BAX recruitment correlates with mitochondrial fission during apoptosis. Sci. Rep. *9*, 16565. https://doi.org/10.1038/s41598-019-53049-w.

46. Jenner, A., Peña-Blanco, A., Salvador-Gallego, R., Ugarte-Uribe, B., Zollo, C., Ganief, T., Bierlmeier, J., Mund, M., Lee, J.E., Ries, J., et al. (2022). DRP1 interacts directly with BAX to induce its activation and apoptosis. EMBO J. *41*, e108587. https://doi.org/10.15252/embj.2021108587.

47. Bordt, E.A., Clerc, P., Roelofs, B.A., Saladino, A.J., Tretter, L., Adam-Vizi, V., Cherok, E., Khalil, A., Yadava, N., Ge, S.X., et al. (2017). The putative Drp1 inhibitor mdivi-1 is a reversible mitochondrial complex I inhibitor that modulates reactive oxygen species. Dev. Cell *40*, 583–594.e6. https://doi.org/10.1016/j.devcel.2017.02.020.

48. Berman, S.B., Chen, Y.b., Qi, B., McCaffery, J.M., Rucker, E.B., Goebbels, S., Nave, K.-A., Arnold, B.A., Jonas, E.A., Pineda, F.J., and Hardwick, J.M. (2009). Bcl-xL increases mitochondrial fission, fusion, and biomass in neurons. J. Cell Biol. *184*, 707–719. https://doi.org/10.1083/jcb.200809060.

49. Flippo, K.H., and Strack, S. (2017). Mitochondrial dynamics in neuronal injury, development and plasticity. J. Cell Sci. *130*, 671–681. https://doi.org/10.1242/jcs.171017.

50. Cao, K., Riley, J.S., Heilig, R., Montes-Gómez, A.E., Vringer, E., Berthenet, K., Cloix, C., Elmasry, Y., Spiller, D.G., Ichim, G., et al. (2022). Mitochondrial dynamics regulate genome stability via control of caspase-dependent DNA damage. Dev. Cell *57*, 1211–1225.e6. https://doi.org/10.1016/j.devcel.2022.03.019.

51. Hand, R., and Polleux, F. (2011). Neurogenin2 regulates the initial axon guidance of cortical pyramidal neurons projecting medially to the corpus callosum. Neural Dev. *6*, 30. https://doi.org/10.1186/1749-8104-6-30.

52. Courchet, J., Lewis, T.L., Lee, S., Courchet, V., Liou, D.-Y., Aizawa, S., and Polleux, F. (2013). Terminal axon branching is regulated by the LKB1-NUAK1 kinase pathway via presynaptic mitochondrial capture. Cell *153*, 1510–1525. https://doi.org/10.1016/j.cell.2013.05.021.

53. Virlogeux, A., Moutaux, E., Christaller, W., Genoux, A., Bruyère, J., Fino, E., Charlot, B., Cazorla, M., and Saudou, F. (2018). Reconstituting corticostriatal network on-a-Chip reveals the contribution of the presynaptic compartment to huntington's disease. Cell Rep. *22*, 110–122. https://doi.org/10.1016/j.celrep.2017.12.013.

54. Wieckowski, M.R., Giorgi, C., Lebiedzinska, M., Duszynski, J., and Pinton, P. (2009). Isolation of mitochondria-associated membranes and mitochondria from animal tissues and cells. Nat. Protoc. *4*, 1582–1590. https://doi.org/10.1038/nprot.2009.151.

STAR★METHODS

KEY RESOURCES TABLE

REAGENT or RESOURCE	SOURCE	IDENTIFIER
Antibodies		
Anti-Vinculin	Santa Cruz	Cat#sc-55465; RRID: AB_630433
Anti-Calnexin	Abcam	Cat#ab22595; RRID: AB_2069006
Anti-F0F1 ATP synthase β	BD Biosciences	Cat#612518; RRID: AB_399819
Anti-Bcl-xL (54H6)	Cell signaling	Cat#2764; RRID: AB_2228008
Anti-Cleaved caspase-3	Cell signaling	Cat#9661; RRID: AB_2341188
Anti-Tau (Tau-5)	Abcam	Cat#ab80579; RRID: AB_1603723
Anti-βIII Tubulin (clone TUJ1)	Biolegend	Cat#801201; RRID: AB_2313773
Anti-Synaptophysin	Abcam	Cat#ab14692; RRID: AB_301417
Anti-PSD95 (clone 7E3-1B8)	Millipore	Cat#MAB1598; RRID: AB_94278
Anti-Actin	Sigma-Aldrich	Cat#A2066; RRID:AB_476693
Anti-VDAC1	Abcam	Cat#ab14734; RRID: AB_443084
Anti-Drp1	Invitrogen	Cat#PA1-16987; RRID: AB_2093523
Anti-Flag	Sigma-Aldrich	Cat#F7425; RRID: AB_439687
Anti-phospho Drp1 Ser616	Cell signaling	Cat#3455; RRID: AB_2085352
Anti-Opa1	BD Biosciences	Cat#612607; RRID: AB_399889
Anti-Mfn2	Cell signaling	Cat#11925; RRID: AB_2750893
Polyclonal goat anti-Rabbit immunoglobulins – HRP	Dako	P0448; RRID: AB_2617138
Goat anti-mouse IgG - HRP	Invitrogen	G21040; RRID: AB_2536527
Chemicals, peptides, and recombinant proteins		
Z-DEVD-FMK	Cayman Chemical	Cat#14414
TMRE	Sigma-Aldrich	Cat#87917
A/C Heterodimerizer	Takara Bio	Cat#635056
m-divi	Sigma-Aldrich	Cat#M0199
WEHI-539	Cayman chemical	Cat#21478
Critical commercial assays		
DABMap Kit	Roche	05266360001
Experimental models: Cell lines		
HeLa	ATCC	CCl-2; RRID: CVCL_0030
Experimental models: Organisms/strains		
Mouse C57/BL6J ER-xL	This paper	N/A
Oligonucleotides		
Primers: EX3-F: GGAAAGGCCAGGAGCGCTTC XTAG-R: CCCAACCCTGTGATAGGGCAAG	IDT-DNA (Leuven)	N/A
Recombinant DNA		
pSCV2	Julien Courchet lab, see Hand and Polleux[51]	N/A
pCAG-mitoDsRed	Julien Courchet lab, see Courchet et al.[52]	N/A
Mito-mCherry-FRB	Gabriel Ichim lab see Ichim et al.[12]	N/A
Cyto-GFP-FKBP	Gabriel Ichim lab, see Ichim et al.[12]	N/A

(*Continued on next page*)

Continued

REAGENT or RESOURCE	SOURCE	IDENTIFIER
pCS2+ Flag Bcl-xL WT	This paper	N/A
pCS2+ Flag Bcl-xL ER	This paper	N/A
pCAG-Drp1 K38A	This paper	N/A
Software and algorithms		
Prism 9	Graphpad	N/A
ImageJ/Fiji	N/A	N/A
Other		
Anti-Flag M2 magnetic beads	Millipore	M8823

RESOURCE AVAILABILITY

Lead contact

Further information and requests for resources and reagents should be directed to and will be fulfilled by the lead contact, Germain Gillet (germain.gillet@univ-lyon1.fr).

Materials availability

All materials generated in this study are available from the lead contact without restriction.

Data and code availability

- The data presented in this article will be made available by the lead contact upon request.
- This paper does not report any original code.
- Any additional information required to reanalyze the data reported in this paper is available from the lead contact upon request.

EXPERIMENTAL MODEL AND SUBJECT DETAILS

Heterozygous ER-xL KI mice were generated on a C57BL/6J background. These mice express mouse Bcl-xL exon 3 with a modified transmembrane domain-containing an ER-targeting Cb5 sequence.

Animal care was in accordance with the recommendation of the European Community and the French National Committee. Animals had access to food and water *ad libitum* and were kept at a constant temperature on a 12-hour light/dark cycle.

To generate embryos for histology and primary neuron experiment, males and females from 6 weeksold were mated for one night. For the subcellular fractionation experiment, brains were extracted from newborn mice. The sex of the animals used in this study (embryos and newborns) was not investigated.

METHOD DETAILS

Ex vivo electroporation

DNA plasmid at 1 μg/μL mixed with 0.5% Fast Green (Sigma, 1:10 ratio) was injected into the lateral ventricles of isolated E15.5 embryonic mouse heads that were decapitated and reserved in complete Hank's Balanced Salt Solution (HBSS) (Life Technologies). Electroporation was performed on the whole head with skull and skin intact, using gold-coated electrodes (GenePads BTX) and the ECM 830 electroporator system (BTX). Electroporation parameters were: five unipolar pulses of 100 ms in length, with a 100 ms interval between each pulse. After electroporation, the brain was immediately used for culture preparation.

Primary cortical neuron culture

Cortices from E15.5 mouse embryos were dissected in sterile complete HBSS (cHBSS) supplemented with HEPES 2.5 mM (Sigma, 11560496), $CaCl_2$ 1 mM (Sigma), $MgSO_4$ 1 mM (Sigma), $NaHCO_3$ 4 mM (Sigma), and D-glucose 30 mM. After dissection, cortical parts were dissociated by incubating with papain 10 units/mL in cHBSS for 15minat 37°C, followed by 1 min of incubation with DNase 1,500 units/mL in cHBSS. After

incubation, cortices were washed three times with cHBSS and mechanically dissociated by repeatedly pipetting in cHBSS. After dissociation, cells were plated at 100,000 cells per 12 mm coverslip or 300,000 cells per 35 mm disk (Ibidi) coated with Poly-D-lysin (0.1 mg/mL, Sigma) in Neurobasal medium supplemented with B27 1x (Life Technologies), N2 1x (Life Technologies), L-glutamine (0.5mM), 2-mercaptoethanol (50 μM), and Penicillin 100units/mL – Streptomycin 100μg/mL, hereafter referred to as complete NB, for 5-7 days. For long-term cultures of 21 days, cells were cultured in complete NB supplemented with fetal bovine serum (5%) for the first 7 days, then the serum-containing medium was gradually replaced by a serum-free medium from day 7 to day 14. From day 14 to 21, medium was changed each 3 days.

Microfluidic chamber preparation

Microfluidic chambers were prepared as previously described.[53] Briefly, microfluidic chambers were made of polydimethylsiloxane (PDMS, Sylgard 184, Dow Corning). A mixture of 10:1 of liquid polymer and curing agent was poured into an epoxy resin mold. The filled molds were incubated under vacuum for 1 h to remove air bubbles, then incubated at 60°C for 3 h. Polymerized PDMS microchambers were pulled out, washed with alcohol 100% with quick passages through an ultrasonic bath, and finally washed with distilled water. Microchambers were dried at 60°C for 30 min. Dry microchambers and 35 mm glass-bottom disks (FluoroDish, WPI) were activated by a plasma cleaner treatment for 30 s. PDMS pieces were immediately fixed on a 35 mm disk. Microchambers were then sterilized under UV light for 30 min. The microchambers were coated with Poly-D-lysine (0.1 mg/mL, Sigma) in the upper and synaptic chamber, and a mixture of Poly-D-lysine (0.1 mg/mL, Sigma) and laminin (10 μg/mL) in the lower chamber overnight at 4°C. The next day, microchambers were washed three times with complete NB and placed at 37°C before plating.

Western blotting

Cells were washed in cold PBS (1X) buffer and then harvested in ice-cold lysis buffer containing 50 mM Tris pH 7.5, 150 mM sodium chloride, 1% NP40, 0.25% sodium deoxycholate, 1 mM EDTA, supplemented with protease inhibitor cocktail (Roche). Proteins were separated by SDS-PAGE and then transferred to the PDVF membrane using Trans-blot® Turbo™ Transfer System. After transfer, the membrane was blocked in 5% milk in trisbuffered saline (25 mM Tris-base pH 7.4, 137 mM sodium chloride, and 2.7 mM potassium chloride) plus 0.1% Tween®20 (TBS-T). After blocking, the membrane was incubated overnight at 4°C with the primary antibody in 5% milk in TBS-T. The next day, the membrane was washed three times with TBS-T and incubated with appropriate Horseradish peroxidase-conjugated secondary antibodies at the ratio of 1:3,000 in TBS-T at room temperature for 1 h. After washing three times with TBS-T, proteins were visualized with Lumi-Light^{PLUS}Western Blotting Substrate (Roche) using ChemiDoc Imaging System (Biorad). Primary antibodies used for Western blot were: Opa1 (1:1,000, BD Biosciences, 612607), Drp1 (1:500, Invitrogen, PA1-16987), Vinculin (1:500, Santa Cruz, sc-55465), VDAC1 (1:1,000, Abcam, ab14734), Actin (1:100, Sigma, A2066), phospho-Drp1 Ser616 (1:1,000, Cell Signaling, 4494), Mitofusin 2 (1:1,000, Cell Signaling, 9482), Bcl-xL (1:1,000, Cell Signaling, 2764), Calnexin (1:1,000, Abcam, ab22595), F0F1 ATPase (1:2000, BD Biosciences, 612518), Flag M2 (1:1,000, Sigma, F3165).

Co-immunoprecipitation

Immunoprecipitation experiments were performed on HeLa cells. Cells at 80-90% confluence in 6-well plates were transfected with 2 μg of pCS2+ empty vector, pCS2+Flag-Bcl-xL WT or pCS2+Flag-Bcl-xL-cb5, using X-tremeGENE™ HP DNA Transfection Reagent (Roche) according to the manufacturer's protocol. After 24 h of transfection, cells were harvested in the TNE buffer (10 mM Tris-HCl, 200 mM NaCl, 1 mM EDTA (pH 7,4), supplemented with 0.2% NP-40, 2.5% sodium pyrophosphate, 0.1% glycerol-2-phosphate, and protease inhibitor). Subsequently, protein extracts were incubated with 20 μL of AntiFlag M2 magnetic beads (Sigma Aldrich) overnight at 4°C. Magnetic beads were then washed three times with TNE buffer and analyzed by immunoblot.

Subcellular fractionation

Subcellular fractionation experiments followed the previously described protocol.[54] Briefly, 8-10 brains isolated from newborn mice were washed twice in the PBS and cut into small pieces in ice-cold MB buffer (210 mM mannitol, 70 mM sucrose, 1 mM EDTA, and 10 mM Hepes(pH 7.4) containing protease inhibitors; Roche). Cells were homogenized and then disrupted using Dounce homogenizers (loose and tight) 4 to 5 times. The homogenized mixture was then centrifuged at 900 *g* to remove nuclei and undisrupted cells and centrifuged at 10,600 *g* to obtain crude mitochondria. The pellet containing crude mitochondria was

suspended in MB buffer and then gently laid on a Percoll medium (225 mM mannitol, 25 mM HEPES (pH 7.4), 1 mM EGTA, and 30% Percol (vol/vol)) and centrifuged for 30minat 95,000 *g* separating the mitochondria-associated membranes (MAMs) from the mitochondria. The supernatant was centrifuged for 1hat 100,000 *g*. After centrifugation, the pellet contained the microsome fraction, and the supernatant contained the cytosol fraction. Subcellular and total fractions were then analyzed by Western blot (as described above). Protein amounts were loaded as follows: total homogenate: 50μg, ER fraction: 10μg, mitochondrial fraction: 5μg, cytosolic fraction: 25μg. This ensured obtain similar levels of fraction indicator marker in each lane (vinculin, calnexin, F0F1 ATPase) for calibration.

TMRE labeling

For measurements of mitochondrial potential, neurons were pre-incubated in complete HBSS for 30minat 37°C, then incubated in 20 nM tetramethylrhodamine ethyl ester (TMRE) in complete HBSS for 30minat 37°C. The medium was then replaced by a 5 nM TMRE solution immediately before live imaging.

Immunofluorescence

Cortical neurons were seeded onto coverslips coated with Poly-D-lysine and laminin (Corning®). Neurons were maintained in culture for 5-21 days, depending on experiments (indicated in each experiment). Cells were then fixed in 4% paraformaldehyde solution for 20 min and washed three times with PBS. Following permeabilization with 3% bovine serum albumin in PBS 0.1% Triton X-100, cells were incubated at room temperature for 1 h with the primary antibodies. Goat anti-mouse or goat anti-rabbit immunoglobulin G Alexa Fluor 488 or 568 were used as secondary antibodies (Molecular Probes) at 1:1,000 dilution for 1 h. Nuclei were visualized using Hoechst 33342 dye (Invitrogen H3570) at 1:10,000 dilution.

Immunofluorescence of microfluidic chambers was performed following the protocol for neuron culture. Incubation with the primary antibodies was performed at 4°C overnight.

For preparing cryosections, brains were isolated from newborn mice and fixed in 4% paraformaldehyde solution. After fixation, brain samples were washed three times with PBS and then cryo-protected with a range of 10%, 20%, and 30% sucrose solutions. Brains were frozen rapidly in OCT medium (TBS), cut into 10 μm-thick slices, and preserved at -20°C. Following 10 min of thawing, brain slices were blocked with Antibody Diluent (Thermofisher, 003118). Slides were incubated at 4°C overnight. Goat anti-mouse or goat anti-rabbit immunoglobulin G Alexa Fluor 488 or 568 were used as secondary antibodies. Slides were then mounted with VECTASHIELD® with DAPI (Vectalabs, H-1200).

The primary antibodies used: cleaved caspase-3 (1:400, Cell Signaling, 9661), βIII-tubulin (1:1,000, Biolegend, 801201), tau (1:200, Abcam, ab80579), PostSynaptic Density Protein 95 (1:1,000, Chemicon®, MAB1598), synaptophysin (1:200, Abcam, ab14692).

Immunohistochemistry

Mouse embryos were collected from euthanized pregnant mice and fixed in a 4% paraformaldehyde solution. After fixation, embryos were rinsed 3 times with PBS and then embedded in a paraffin block. Embryo paraffin blocks were then sectioned at a 4-μm thickness and transferred onto glass slides. For immunohistochemistry, embryo sections were deparaffinized by xylene and re-hydrated by dipping in 100%, 95%, 70%, and 50% alcohol. Epitope retrieval was conducted using a Tris-EDTA buffer pH 7.8 for 36 min. Slide sections were then incubated with the primary antibody cleaved caspase-3 (1:400, Cell Signaling, 9664) at 37°C for 1 h. Goat anti-rabbit was used as a secondary antibody (1:300, Vector BA1000). Signals were visualized using the DABMap kit (Roche, 05266360001). Immunohistochemistry steps were performed in the Roche Discovery XT system.

Mitochondrial permeabilization detection

E15.5 embryo cortex was electroporated with Cyto-GFP-FKBP and Mito-mCherry-FRB (ratio 3:1). Subsequently, cortical neurons were isolated and cultured for 7 days. At DIV7, cortical neuron culture was treated with A/C heteromerizer 0.5 μM for 1h. at 37°C, 5% CO_2. After treatment, neurons were fixed with PFA 4% for 15minat 37°C, 5% CO_2.

Image acquisition and analysis

Confocal images were acquired on a Zeiss LSM 880 system equipped with Airyscan, with these lense objectives: 10x AN 0.45, 20x AN 0.8, and 63x AN 1.4. For axonal morphogenesis analysis, we performed a large-field acquisition of a 4×4 tiling scan using a 20x objective. All neurons on the reconstituted image were quantified, and axon length was measured using ImageJ.

During live imaging, the temperature was maintained at 37°C and CO_2 at 5% v/v.

QUANTIFICATION AND STATISTICAL ANALYSIS

Statistical analyses were performed using Prism (GraphPad). The normality test was performed using the Shapiro-Wilk test. Statistical tests and the number of replicates are indicated in the figure legends.